Cell Reports

Resource

A disease-driver population within interstitial cells of human calcific aortic valves identified via single-cell and proteomic profiling

Graphical abstract

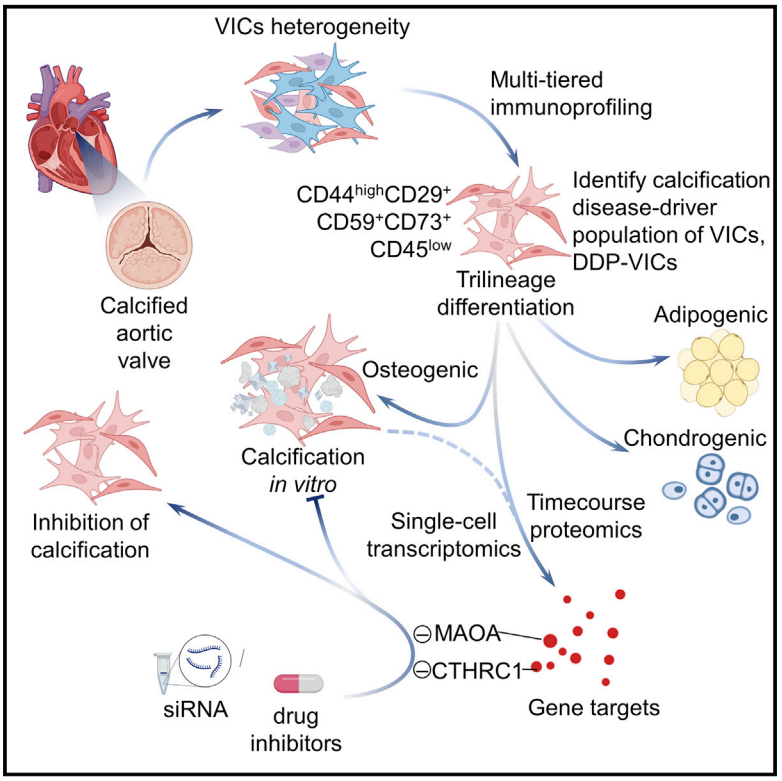

Highlights

- CD44^{high}CD29^{+}CD59^{+}CD73^{+}CD45^{low} cells are disease-driving population (DDP) VICs in CAVD
- DDP-VICs possess osteogenic differentiation properties
- Single-cell analysis and proteomics identified CAVD targets like MAOA and CTHRC1
- MAOA and CTHRC1 inhibition attenuate calcification in human aortic VICs

Authors

Julius L. Decano, Yukio Iwamoto, Shinji Goto, ..., Sasha A. Singh, Masanori Aikawa, Elena Aikawa

Correspondence

eaikawa@bwh.harvard.edu

In brief

Decano et al. characterize valvular interstitial cells (VICs) that are CD44^{high}CD29^{+}CD59^{+}CD73^{+}CD45^{low} within human calcific valve disease (CAVD) as a disease-driver population (DDP) capable of osteogenic and procalcific differentiation. Phenotype-guided single-cell, multi-omic analysis identifies potential CAVD key regulators, such as MAOA and CTHRC1, validated through *in vitro* loss of function and histology.

Decano et al., 2022, Cell Reports *39*, 110685
April 12, 2022
https://doi.org/10.1016/j.celrep.2022.110685

CellPress

Cell Reports

CellPress
OPEN ACCESS

Resource

A disease-driver population within interstitial cells of human calcific aortic valves identified via single-cell and proteomic profiling

Julius L. Decano,[1,5] Yukio Iwamoto,[1,5] Shinji Goto,[1] Janey Y. Lee,[1] Joan T. Matamalas,[1] Arda Halu,[1] Mark Blaser,[1] Lang Ho Lee,[1] Brett Pieper,[1] Sarvesh Chelvanambi,[1] Jessica Silva-Nicolau,[1] Francesca Bartoli-Leonard,[1] Hideyuki Higashi,[1] Haruki Shibata,[1] Payal Vyas,[1] Jianguo Wang,[1] Elena Gostjeva,[2] Simon C. Body,[3] Sasha A. Singh,[1] Masanori Aikawa,[1,4] and Elena Aikawa[1,4,6,*]

[1]Cardiovascular Medicine, Center for Interdisciplinary Cardiovascular Sciences, Brigham and Women's Hospital, Harvard Medical School, Boston, MA 02115, USA

[2]Massachusetts Institute of Technology, Cambridge, MA 02139, USA

[3]Boston University School of Medicine, Boston, MA 02118, USA

[4]Cardiovascular Medicine, Center for Excellence in Vascular Medicine, Brigham and Women's Hospital, Harvard Medical School, Boston, MA 02115, USA

[5]These authors contributed equally

[6]Lead contact

*Correspondence: eaikawa@bwh.harvard.edu

https://doi.org/10.1016/j.celrep.2022.110685

SUMMARY

Cellular heterogeneity of aortic valves complicates the mechanistic evaluation of the calcification processes in calcific aortic valve disease (CAVD), and animal disease models are lacking. In this study, we identify a disease-driver population (DDP) within valvular interstitial cells (VICs). Through stepwise single-cell analysis, phenotype-guided omic profiling, and network-based analysis, we characterize the DDP fingerprint as $CD44^{high}CD29^{+}CD59^{+}CD73^{+}CD45^{low}$ and discover potential key regulators of human CAVD. These DDP-VICs demonstrate multi-lineage differentiation and osteogenic properties. Temporal proteomic profiling of DDP-VICs identifies potential targets for therapy, including MAOA and CTHRC1. *In vitro* loss-of-function experiments confirm our targets. Such a stepwise strategy may be advantageous for therapeutic target discovery in other disease contexts.

INTRODUCTION

Human aortic valve calcification is the leading cause of fatal aortic stenosis (Stone et al., 2014). Initially considered a degenerative pathology, it is currently viewed as a biologically active process, with a spectrum ranging from aortic sclerosis to overt calcific aortic valve disease (CAVD) (Aikawa and Libby, 2017). An ever-increasing aging population brings along an increase in severe CAVD rates. Left untreated, severe CAVD leads to heart failure and death. No effective drug therapy is available; invasive surgical or transcatheter aortic valve replacements remain the sole treatment options (Iung et al., 2003).

Our recent study successfully identified molecular regulatory networks in CAVD by multi-omic approaches on a layer and disease-stage basis (Schlotter et al., 2018). Valvular interstitial cells (VICs) in normal valves maintain matrix integrity and compartmentalization (Aikawa and Libby, 2017; Hinton et al., 2006). The current paradigm suggests that VICs are a plastic cell population, and in disease conditions, VICs differentiate into activated collagen-producing myofibroblast-like cells contributing to matrix remodeling and fibrosis (Rabkin et al., 2001). However, whether a specific subpopulation of VICs responsible for initiation of the calcification process exists is unclear. Inspired by the emerging concept of cell heterogeneity in cardiovascular disease (Decano and Aikawa, 2018; Decano et al., 2021), we used a combination of high-throughput profiling technologies to test our hypothesis that a specific disease-driver population (DDP) capable of osteogenic differentiation is present in human CAVD.

RESULTS

Shared top-expressing cell surface markers in MSCs and VICs

We hypothesized that a progenitor-like VIC subpopulation may drive calcification in human CAVD. Using mesenchymal stem cells (MSCs) (cell line from the American Type Culture Collection [ATCC]) as the progenitor reference control, pooled VICs from 8 donors were immediately processed for high-throughput screening-flow cytometric (HTS-FC) analysis of 242 surface proteins (Figure 1A; Table S1). A shared high expression of markers among (1) diseased VICs, (2) undifferentiated MSCs (MSC-NM), (3) MSCs differentiated toward osteogenic (MSC-OM), and (4) adipogenic (MSC-AM) phenotypes (Figure 1A) is percentile

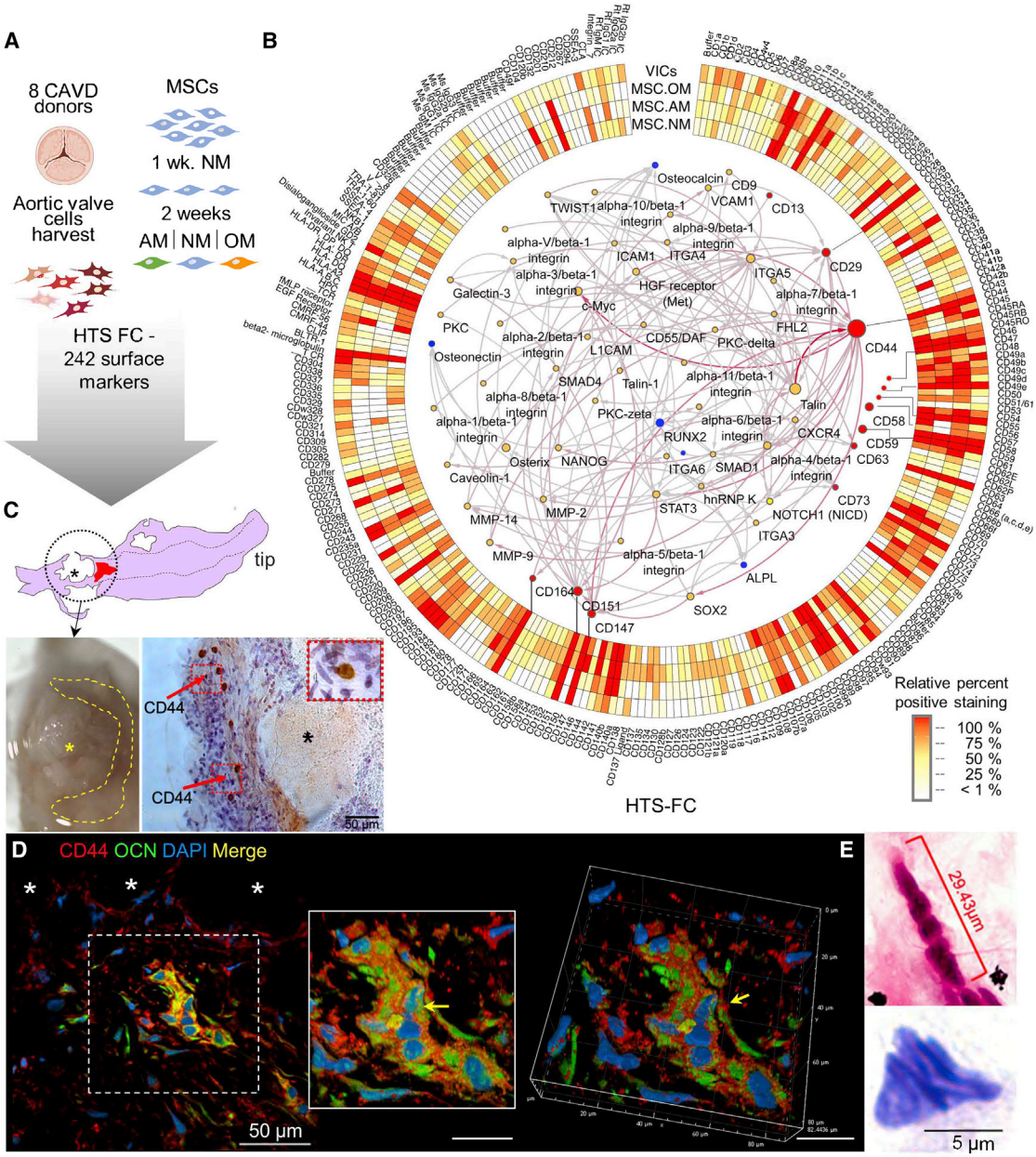

Figure 1. Surface markers for putative disease driver VIC populations in CAVD

(A) HTS-FC of freshly isolated VICs (n = 8 CAVD patients, pooled) and MSCs cultured for 2 weeks in normal media (NM), osteogenic media (OM), or adipogenic media (AM).

(B) HTS-FC expression heatmap of VICs and MSCs (percent positive staining) with corresponding first-neighbors PPI network nested within. Blue nodes, seeded target genes; red source nodes, surface markers with high expression in all 4 cell conditions; yellow nodes, first and second neighbors connecting the seeded and surface marker genes. Node size reflects the degree of hub centrality (betweenness centrality).

(C) Leaflet schema of an area close to calcification (*). Tissue cell spread technique applied to area with calcification nodule (*); n = 4 valve donors. CD44 IHC after tissue spread showing $CD44^+$ cells (red arrows and inset) close to calcification (*).

(D) Immunofluorescence of a region near calcification. CD44 (red) and osteocalcin (OCN) (green) co-localization (yellow) among cells containing atypical nuclear morphology. Cells with cupped nuclei (DAPI staining, yellow arrow) near calcification with $CD44^+$ staining.

(E) Feulgen staining of nuclei appearing as "spherical beads in series" (top image) or as "stacked bell-shaped cups" (bottom). PPI, protein-protein interaction; IHC, immunohistochemistry.

ranked based on percent positive staining (isotype controls used; Figure S1A) for each surface marker (Table S1). The previously reported MSC markers' percent positive cutoff (85%) is used (Walmsley et al., 2015). The 17 surface markers that consistently scored >85% in all groups are MSC-normal media (NM), MSC-osteogenic media (OM), MSC-AM, the VICs CD13, CD29, CD44, CD47, CD49e, CD55, CD58, CD59, CD63, CD73, CD147, CD151, CD164, beta2-microtubulin, human leukocyte antigen (HLA) A-B-C, and HLA-B2. In contrast, the CD38- and CD45-percent positive fractions differ across the 4 conditions (Table S1). CD38 and CD45 are prototypical leukocyte markers (Mason and Gatter, 1987).

Using network analysis, we investigated how the 16 surface proteins are associated with calcification-related molecules. Beta2-microtubulin, HLA A-B-C, and HLA-B2 are excluded from the analysis due to ubiquitous expression in all of the cells (Dimitrios and Monos, 2018). The flow cytometry-derived cell expression profile is rendered in a circular heatmap (Figure 1B), and the remaining 13 surface proteins are projected onto a curated protein-protein interaction (PPI) network (STAR Methods). This directional interactome network (Figure 1B, inner panel) is anchored to calcification by using 4 known calcification markers (osteocalcin, tissue-nonspecific alkaline phosphatase [ALPL], RUNX2, and osteonectin) as "target" nodes (blue nodes, Figure 1B) (Chellan et al., 2018; Millar et al., 2017) and each CD marker as a "source" node (red node, Figure 1B). We then find the "linking" protein to connect the source and target nodes (MetaCore, Clarivate). The linking proteins included NANOG, a stem-cell proliferation marker (Boyer et al., 2005). With these links, we ranked the 13 source nodes based on network topology prioritization measures of betweenness centrality and edge count, revealing CD44 as the central hub node (Figure S1B).

CD44^{+} VICs are distributed near calcification regions in aortic valve leaflets

Immunohistochemistry (IHC) on aortic valve leaflet sections from CAVD patients (n = 10) revealed the relative location of the heterogeneous VICs. We assessed progenitor (Nomura et al., 2013; Walmsley et al., 2015), osteogenic (Yu et al., 2010), and fibroblastic (Rabkin et al., 2001) markers in longitudinal cross-sections of the leaflets: CD34, CD44, CD45, CD73, CD90, CD105, CD133, CD146, NANOG, C-Kit, osteocalcin, and vimentin. To characterize the layer-specific marker distributions, we divided histology scans of the stained leaflet cross-sections into the 3 layers (fibrosa, spongiosa, and ventricularis); we then used a Python script to quantify IHC-marker staining (Method details). Note that the fibrosa layer is more calcification prone than the ventricularis (Schlotter et al., 2018). An interlayer comparison examining percent-positive staining cells for the markers mentioned is then conducted (representative valve shown, Figure S1C). CD44 showed the highest percent-positive staining among all cells in the fibrosa layer. In contrast, its relative expression decreased in the ventricularis layer ($p < 0.0001$; Figure S1D). This pattern of decreasing expression from the calcification-prone region toward the non-calcified region is absent with any other tested markers (Figure S1D).

CD44^{high} VICs are functionally and spatially associated with areas of calcification

Areas in which CD44 expression colocalizes with calcification are examined by performing a tissue-spread technique IHC (Gostjeva et al., 2009) (Figure 1C, n = 4 donors). This type of IHC preserves 3D tissue architecture, unlike routine histological sectioning-based methods. After dissecting the peri-calcification region (Figure 1C), tissue cell spread digestion and CD44 immunostaining are completed. CD44-expressing cell clusters appear near microcalcification (representative image, Figure 1C), with some cells expressing osteocalcin (Figure 1D). We observe that the cells with CD44 and osteocalcin signals also harbor atypical nuclear morphology (Figures 1D, 1E, and 2A–2C). These nuclei may appear as beads in a series (Figures 2B and 2C, arrows) or stacked bell-shaped cups (Figures 1E and 2A, arrows), reminiscent of metakaryotic progenitor cells found during human organogenesis (Gostjeva et al., 2009). This suggests that CD44^{+} VICs with atypical-shaped nuclei may be part of a pool of progenitor cells.

An increase in nuclear area may signify cells progressing through the cell cycle (Chu et al., 2017), such as proliferating progenitor cells. Similarly, nuclei in pluripotent cells are more plastic and deformable in shape and size than fully differentiated adult cells owing to their tendencies for cell division and chromatin reorganization (Pajerowski et al., 2007). Given the aforementioned atypical nuclear appearance, we quantified the differences in nuclear morphology between the progenitor-like VICs (atypical nuclei) and the mature differentiated VICs (typical-looking nuclei). Using CellProfiler (McQuin et al., 2018) (https://cellprofiler.org), we measured the area, compactness, and eccentricity of the nuclei (Figures 2D–2F). Compactness is the variance of the radial distance of the pixels of the object from the centroid divided by the area. A smooth circular nucleus has a compactness of 1.0, while an elongated spindle-shaped nucleus has a higher compactness number as defined by CellProfiler. Eccentricity ranges from 0 to 1, with an ellipse having a score of 1 (Figure 2G). We sampled and analyzed regions proximal to calcification (having VICs with atypical-looking nuclei, Figure 2D) and cells distal to calcifications (having VICs with typical elliptical-shaped nuclei) (Figure 2E). VICs from 8 healthy valve donors have also been included (Figure 2F).

Wilcoxon nonparametric rank-sum statistics (Method details) reveal significant differences between the 3 groups of VICs on all 3 metrics (Figures 2G–2J). As observed, the progenitor-like cell nuclear area tended to be larger, but with higher size (area) heterogeneity (Figure 2H), which may indicate the varying states of chromosomal activity (Jevtić et al., 2014). In addition, progenitor-like VICs appear to have nuclei linked together in a "daisy-chain" series. Each linked nucleus is more rounded than regular VICs from CAVD and non-diseased valves, which have single elongated spindle-shaped nuclei (Figures 2E and 2F).

The calcification potential of tissue-derived and fluorescence-activated cell sorting (FACS)-sorted CD44^{+} VICs was then examined. The CD44^{high} VICs within the general CD44^{+} cell population was detected (Figure 3A). We sorted both CD44^{+} gated VICs (allophycocyanin [APC] mean intensity fluorescence [MIF] $\geq 10^{3}$) and CD44^{high} VICs (APC MIF $\geq 10^{4}$). The CD44^{high}, CD44^{+},

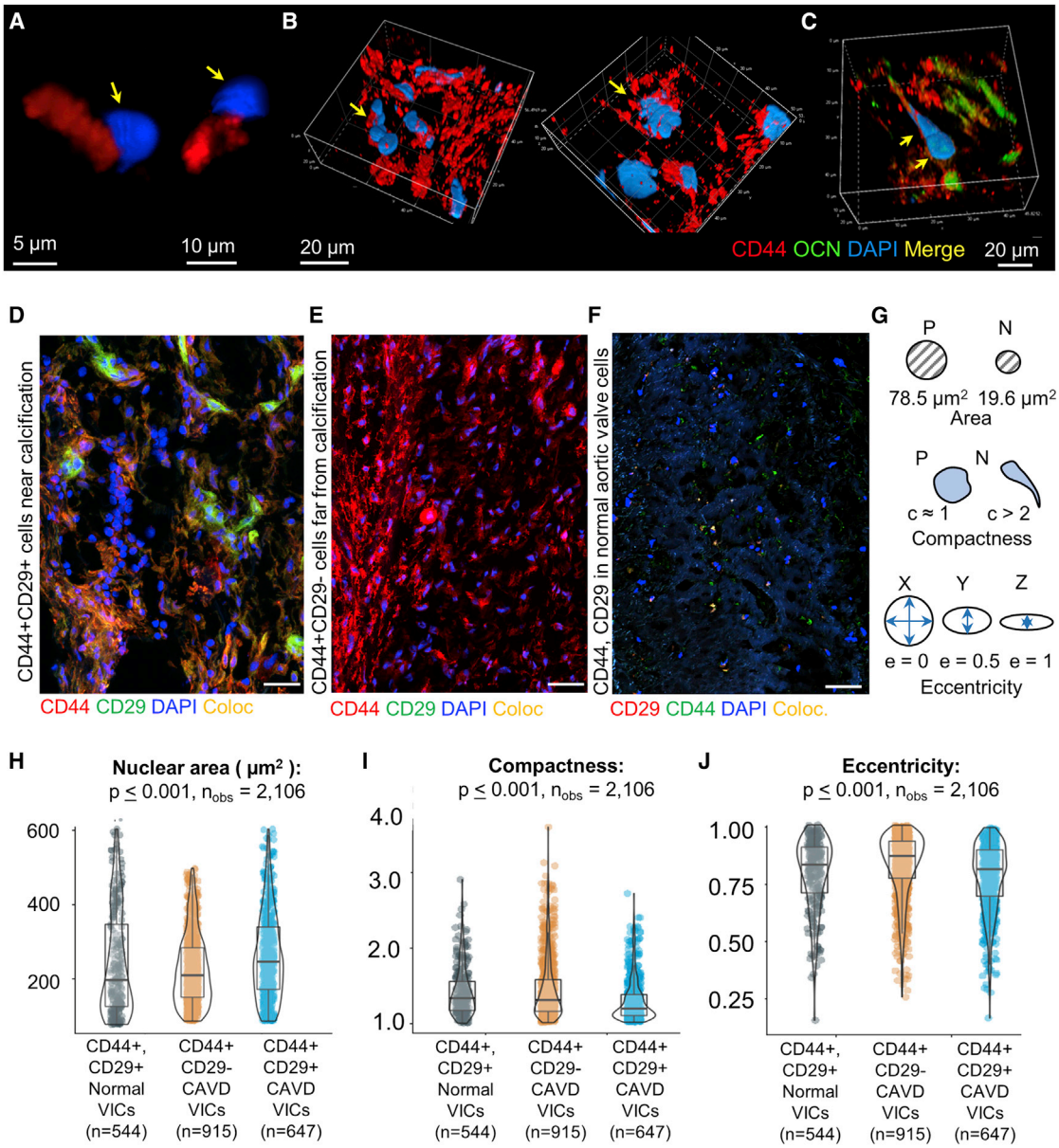

Figure 2. High content imaging of putative DDP (progenitors) VIC nuclei compared with non-progenitors

(A–C) CD44$^+$ staining and atypical metakaryotic nuclei either in (A) stacked cups configuration or in (B and C) serial configuration (yellow arrows), rendered from z stack.

(D) Immunofluorescence (IF) staining of PE-CD44 (red) and AF488-CD29 (green) of areas near calcification (scale bar, 50 μm), n = 5. The majority of cells stain with CD44 and CD29, representative images.

(E) CD44$^+$ cells distant from calcification. None co-stained with CD29; n = 5.

(F) Cells from normal valve sections and CD44 and CD29 staining, few are double positive; n = 4.

(G) Definitions for area, compactness, and eccentricity.

(H–J) Area (in pixels) (H), compactness (I), and eccentricity (J) of the nuclei comparison. n = 4–5 donors per group. Statistical testing of the (H)–(J) group comparison (progenitor-like, CD44$^+$ CD29$^+$ near calcification compared with non-progenitor-like, CD44$^+$ CD29$^-$ and distal to the calcific area versus normal valve cells) is a Wilcoxon non-parametric rank-sum statistic. p value denotes statistical significance on paired group comparison. n_{obs} = number of observations.

and unsorted mixed population VICs were cultured in normal media (NM) and two pro-calcifying media conditions: OM and high phosphate media (PM). OM is an ALP-dependent (Nishimura et al., 2015), while PM is an ALP-independent (Schlotter et al., 2018), mineralizing condition. After 21 days of culture, cells are stained for calcium deposition (Alizarin Red S). CD44^{high} and CD44$^+$ VICs calcify under both OM and PM conditions, but not in NM. CD44^{high} VICs calcify more readily than CD44$^+$ VICs (Figure 3A). The unsorted mixed (MIX) VIC population only calcifies in PM conditions. At 3 weeks, CD44 small interfering RNA

CellPress
OPEN ACCESS

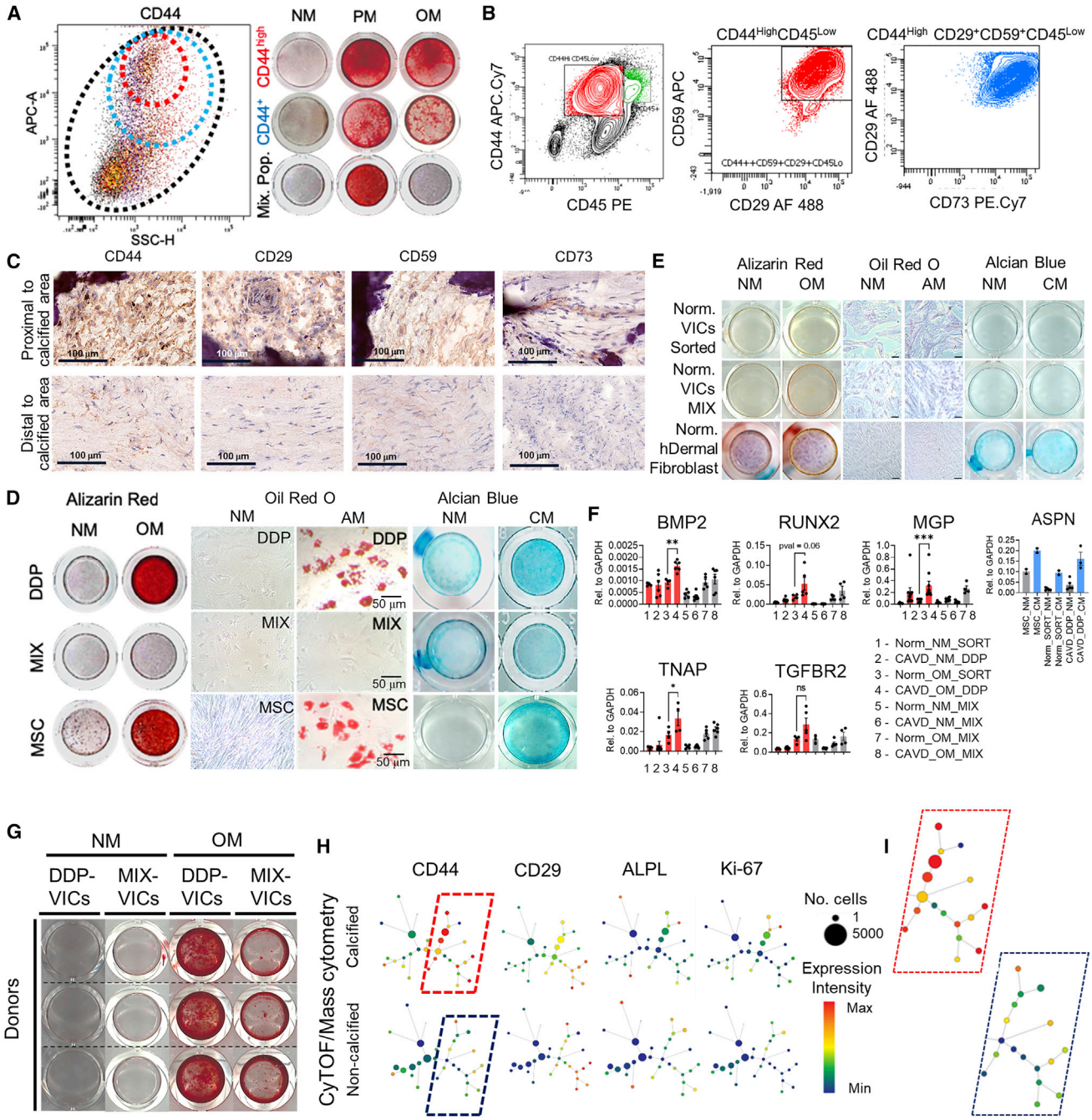

Figure 3. Identifying the disease driver population in CAVD

(A) Representative image of FACS-sorted aortic VICs cultured in normal media (NM), high phosphate media (PM), or osteogenic media (OM). Unsorted VICs (mix), sorted CD44^{high}, and sorted CD44^{+} cells calcified under OM and PM conditions (PM > OM), but not in NM; Alizarin Red staining at day 21 (n = 3).

(B) Multicolor flow cytometry shows co-localization of CD44^{high} VICs with CD29^{+}, CD59^{+}, and CD73^{+} staining, with lower staining of CD45; n = 3 donors.

(C) Immunohistochemistry of areas proximal to calcification show more abundant staining of markers CD44, CD29, CD59, and CD73 than in areas more distal to the calcification (n = 3).

(D) Sorted VICs population CD44^{high}CD29^{+}CD59^{+}CD73^{+}CD45^{low} cells readily differentiated into calcifying osteoblast-like cells in OM (Alizarin Red staining) and fat droplet-containing adipocyte-like cells in AM (Oil Red O) similar to MSCs differentiation in the same media. Alcian blue staining of chondrocyte-like DDP VICs in CM. Mixed (MIX) unsorted aortic VICs show no comparable differentiation in OM, CM, or AM; n = 4 donors.

(E) Normal aortic VICs, CD44^{high}CD29^{+}CD59^{+}CD73^{+}CD45^{low} sorted (SORT) and unsorted (MIX) mixed, differentiates on OM, CM, and AM with no considerable change at 2 weeks. Adult normal human dermal fibroblasts are used as normal fibroblast reference.

(legend continued on next page)

(siRNA)-treated VICs cultured in PM media reduce calcification comparable to NM (Figure S1E).

Osteogenic CD44^{high} cells co-express CD29, CD59, and CD73 progenitor markers

Thus far, our findings demonstrate that higher calcification potential associates with CD44 expression in VICs. We used a literature citation abstract review to expand this progenitor-like and calcification-prone VIC population. We examined all 13 (source nodes) HTS-FC-identified markers (Figure 1B) for associations with the terms (1) ''mesenchymal stem cells,'' (2) ''mesenchymal progenitor cells,'' and (3) ''calcification'' (Method details). The 8 most highly cited markers on abstracts citing mesenchymal stem cells or mesenchymal progenitor cells are CD44, CD73, CD29, CD13, CD55, CD49e, CD147, and CD59 (ordered from high to low; Figure S1F, left). For markers overlapping with the term ''calcification,'' the ranking is CD29, CD44, CD13, CD63, CD73, CD59, CD55, and CD49e (Figure S1F, right). The overlap of the 2 lists yielded CD44, CD29, CD13, CD73, CD55, CD59, and CD49e (a CD29 binding partner). Therefore, we assayed the coexpression of these 7 markers in CD44^{high} VICs using multi-parameter (color) flow cytometry (n = 3 donors). As a control for a non-mesenchymal-derived cell type, we monitored the leukocyte marker CD45 (Albanese et al., 2017). We found that the CD44^{high} population is positive for CD29, CD59, and CD73 (Figure 3B) and negative for CD13 and CD55 (Figure S1G). Isotype antibody controls are used for reference (Figure S1H). All of the tested VIC populations exhibit low staining for CD45 (Figure 3B). Immunohistochemistry (IHC)-based quantitative distance from calcification mapping of CD44, CD29, CD59, and osteocalcin-positive cells show a higher expression of these markers when in proximity to calcification nodules (Figures S2A–S2D). We thus define our progenitor-like VIC population with high calcification potential as CD44^{high}CD29^{+}CD59^{+}CD73^{+}CD45^{low}.

Aortic leaflet cryosections from 3 donors were then immunostained for CD44, CD29, CD59, and CD73. In addition, IHC for osteocalcin, α-smooth muscle actin (α-SMA) (myofibroblast marker), and Ki67 (a nuclear marker of cellular proliferation; Ciceri et al., 2016) was performed. VICs proximal to calcification are immunoreactive for CD44, CD59, CD29, CD73 (Figure 3C), Ki-67 (Figure S2E), and osteocalcin (Figure S2F). Previously assessed proximity measures were quantitated by distance mapping from the calcification (see whole valve section and diagram, Figure S2G). CD44^{+}CD29^{+} VICs expanded *in vitro* also colocalize with vimentin (Figure S2H). Overall, these results demonstrate that VICs in CAVD contain a CD44^{+} subpopulation with high calcification potential and that it includes a subset of VICs that are characterized as the CD44^{high}CD29^{+}CD59^{+}CD73^{+}CD45^{low} phenotype.

The CD44^{high}CD29^{+}CD59^{+}CD73^{+}CD45^{low} VIC phenotype mimics MSC-like properties *in vitro*

We then tested the pluripotency of this VIC subpopulation, designated as the DDP (DDP-VICs), in contrast to the unsorted heterogeneous VICs designated as a mixed population (MIX-VICs). From additional CAVD leaflets (n = 9 donors), we isolated, sorted, and cultured DDP-VICs and MIX-VICs and used MSCs as control. Cells were cultured in OM, AM, chondrogenic (CM), or NM (Figure 3D) for 3 weeks to demonstrate trilineage differentiation. Alizarin Red, Oil Red O, and Alcian blue staining detected osteogenic, adipogenic, and chondrogenic differentiation, respectively, for both DDP-VICs and MSC populations, but not for the MIX-VICs. These findings suggest that CD44^{high}CD29^{+}CD59^{+}CD73^{+}CD45^{low} DDP-VICs possess pluripotent progenitor cell-like properties with high osteogenic potential. Non-diseased valve cells, CD44^{high}CD29^{+}CD59^{+}CD73^{+}CD45^{low} sorted and mixed populations, and adult normal fibroblasts (human dermal fibroblast primary cell line) served as the control, and did not differentiate into the OM, AM, and CM lineages (Figure 3E). Osteogenic genes BMP2, RUNX2, TNAP, TGFRB2, and GWAS-associated calcification gene MGP are also increased mainly among the CAVD DDP-VICs samples (Figure 3F). DDP-VICs from CAVD valves calcify more readily than do MIX-VICs (Figure 3G).

Mass cytometry verifies DDP-VIC progenitor-like phenotype

We used mass cytometry (CyTOF) to evaluate more phenotypic features of the DDP-VICs by comparing calcified versus non-calcified regions of aortic valve leaflets (Figure S3A). VICs were isolated from the calcified and non-calcified portions of CAVD leaflets (n = 4). We stained the cells with 11 recently reported intracellular markers of CAVD (Schlotter et al., 2018) (ALPL, α-SMA, glial fibrillary acidic protein [GFAP], Ki-67, NANOG, osteocalcin, pS6, sortilin, transforming growth factor-β [TGF-β], vascular endothelia [VE]-cadherin, and vimentin) and 8 surface antibodies (CD29, CD34, CD44, CD45, CD59, CD63, CD73, and CD105) for subsequent CyTOF (Figure S3B).

Spanning-tree progression analysis of density-normalized events (SPADE) visualization (Qiu, 2017) demonstrates several cell clusters based on their expression profile, represented as nodes (Figure 3H). Each node color represents the level of immunostaining. We identified a specific cell cluster containing DDP-VICs by comparing the CD29, CD44 (Figure 3H), CD59, and CD73 (Figure S3B) expressions in calcified and non-calcified regions of the leaflets. The cluster of VICs marked by trapezoidal boxes in Figure 3H and shown enlarged in Figure 3I demonstrates that calcified SPADEs contained more VICs with higher expression (larger nodes with warmer colors) of CD29, CD44, ALPL, and Ki67 (Figure 3H), as well as CD59 and CD73

(F) Bulk gene expression of osteogenic differentiation markers by qPCR of sorted and unsorted VICs from normal and CAVD valves; n = 3 biological replicates with technical duplicates, during NM or OM differentiation. ASPN expression in sorted cells from normal and CAVD valves with MSC as a reference. Cells are grown in either NM or OM, n = 3.

(G) DDP VICs and MIX VICs cultured in either NM or OM media showed early calcification at 2 weeks; n = 3 donors).

(H) CyTOF: comparison of relative expression (warm/red = high to cool/blue = low scale) of ALPL (early calcification marker), CD44, CD29, and Ki67 between calcified and non-calcified portions of valves with mass cytometry; n = 3 donors.

(I) SPADEs of calcified leaflets contained more cells (larger node circles) with higher expression when compared to non-calcified SPADEs, shown through larger nodes with warmer colors versus smaller nodes with cooler colors (insets). ns $p > 0.05$, *$p \leq 0.05$, **$p \leq 0.01$, ***$p \leq 0.001$. Bar graphs are means ± SEMs.

(Figure S3B) when compared to non-calcified SPADEs (smaller nodes with lower expression). NANOG, osteocalcin, pS6, sortilin, TGF-β, and CD34 also showed higher relative expression in the calcified samples, while α-SMA, GFAP, VE-cadherin, vimentin, CD45, CD63, and CD105 demonstrate no difference in calcified compared with non-calcified SPADEs (Figure S3B). These results suggest the predominance of osteogenic (e.g., osteocalcin, sortilin, TGF-β), proliferative (e.g., NANOG, pS6), and progenitor-like (e.g., CD34) cell populations in the calcified leaflet portion.

Single-cell RNA sequencing (scRNA-seq) identifies highly expressed genes during the osteogenic transition of DDP-VICs

We studied the single-cell gene expression of DDP-VICs, MIX-VICs, and MSCs during osteogenic differentiation. Single cells from 6 conditions cultured for 2 weeks (to capture early mRNA changes before peak phenotype on day 21) in NM and OM (MIX-NM, MIX-OM, DDP-NM, DDP-OM, MSC-NM, and MSC-OM) were isolated (Figure 4A) for scRNA-seq (Zilionis et al., 2017) (Method details). The following are cell counts per condition: MIX-NM (n = 1,813), MIX-OM (n = 2,000), DDP-NM (n = 1,814), DDP-OM (n = 2,000), MSC-NM (n = 873), and MSC-OM (n = 2,000). The range of gene reads per cell is from 1,000 to 8,192. Principal-component analysis (PCA) and t-distributed stochastic neighbor embedding (tSNE) plots of the combined transcriptomics data revealed that the MSC-NM and MSC-OM form distinct clusters non-overlapping with other VIC clusters (MIX-NM, MIX-OM, DDP-NM, and DDP-OM) (Figure S4A). This distinct MSC and VIC sample separation (PCA and tSNE) suggests that their global transcriptome is substantially different and cannot be subjected together in downstream co-clustering algorithms (e.g., k-means). We, therefore, analyzed the MSC and VIC datasets separately to characterize the subpopulations (Figures 4B–4E) further. The lack of MSC/VIC cluster overlap may imply substantial cell-type differences that drive the global transcriptome difference. However, exploring MSC behavior during OM stimulation could allow us to capture shared differentially expressed genes (DEGs) with the OM-stimulated DDP-VICs or DEGs that are part of a shared pathway.

tSNE plots visualized k-means clustering of MSC-NM and MSC-OM single-cell expression (intensity) data (6 clusters; Method details). The tSNE plots demonstrate that the MSC-OM population is more heterogeneous than that of MSC-NM since it separated into 5 subclusters (k1, k3, k4, k5, and k6) compared to the single cluster (k2) depicting the entire MSC-NM population (Figures 4B and 4C). In contrast, the degree of heterogeneity across all 4 VIC sample conditions is similar (Figures 4D and 4E). We initially calculated the DEGs between MSC-NM and MSC-OM agnostic of the k-cluster groupings. Then, the relative gene expression of the identified DEGs was mapped onto an expression heatmap of the k-cluster groupings (Figure 4F). Subsequent hierarchical clustering and statistical filtering for those with an increased fold change of $\geq$1.5 at q $\leq$ 0.05 relative to the MSC-NM was done. Of the 5 k-clusters belonging to the MSC-OM condition, k4 exhibits the highest expression levels in most of these increased MSC-OM DEGs, including a known osteoblast-associated marker, SPARC (Ciceri et al., 2016) (Figures 4F, red arrow, and S4B). The merit of single-cell analysis lies in the comparison of subgroup transcriptome (k-clusters) coming from a broader sample-condition DEG comparison (e.g., MSC-OM versus MSC-NM). This way, the genes that differentiate the k4 cluster from the other MSC-OM k-clusters enrich more MSC-OM-prominent genes that are also increased relative to a non-osteogenic condition, MSC-NM (Figure 4F). We then calculated the increasing DEGs between k4 (MSC-OM) and k2 (MSC-NM majority k-cluster) at FC $\geq$ 1.5, q $\leq$ 0.05, generating 49 DEGs (Table S2), including osteoprotegerin (osteoclastogenesis inhibitory factor/TNFRSF11B), osteonectin (SPARC), SPOCK1, elastin, Thy-1 (CD90), and several collagen-related proteins (CTHRC1, COL1A1, COL1A2, COL3A1, COL4A1, COL5A1, and COL5A2).

Next, we compared VIC-OM with VIC-NM (Figures 4D and 4E). VIC-OM comprises DDP-VIC and MIX-VIC samples in OM media (DDP-OM and MIX-OM), while VIC-NM is the combined DDP-VIC and MIX-VIC in NM media. Similarly, we analyzed these samples using PCA, tSNE, and k-means clustering. The VIC-OM k-clusters (Figure 4D) contain DDP-OM and MIX-OM cells in varying numbers (Figure 4E). These cells are clustered together in the same k-cluster because of their overall gene expression similarity. By comparing combined clusters of VIC-OM (k4, k5, and k6) with combined clusters of VIC-NM (k1 and k2) (fold change >1.5, q < 0.05), we identified 18 increased DEGs in the VIC-OM (Table S3). These genes are PHACTR2, HIF-1A, elastin, and collagen-related proteins COL8A1 and CTHRC1. The osteoblast differentiation marker TGF-β receptor 2 (TGFBR2) (Iwata et al., 2010) is also increased among the VIC-OM (Figure S4C).

Subsequently, we filtered for DEGs from the clusters containing VIC-OM cells (k3–k6) compared to the clusters containing only VIC-NM (k1, k2) (Table S2). We included the k3 cluster among VIC-OM clusters despite containing cells from NM stimulation (Figure 4E) because OM cultured cells predominate in this cluster compared to NM-cultured cells. However, it is worth noting that the k4 cluster comprises mostly DDP-OM cells (Figures 4D and 4E). DDP-OM has a higher osteogenic potential than MIX-OM (Figure 4D). The k4 cluster also has more cells with higher expression of ALPL (Figure S4D) and genes related to noncanonical WNT signaling, which is important in aortic valve calcification (Albanese et al., 2017) (Figure S4E) compared to k5 and k6 clusters, which are MIX-OM predominant (Figures 4D and 4E). Using pathway enrichment, we identified the k4 cluster as having the most pathways related to stem cell differentiation and TGF-β signaling (Table S2). Therefore, we were interested in k4 DEGs with $\geq$1.5-fold change over k1 and k2 combined clusters (Table S2), which are almost entirely composed of MIX-NM and DDP-NM, yielding 34 DEGs (Figure 4G; Table S2). These genes include MAOA, PHACTR2, TGFRB2, HIF-1A, elastin, and collagen regulation-associated proteins (COL8A1, lysyl oxidase, CTHRC1). Both MSC-OM k4 and DDP-OM k4 cluster-specific gene lists are enriched for biological processes and pathways. As a result, these turned out to be related to pathways driving the calcification process (Table S2), such as extracellular matrix (ECM) remodeling, TGF-β-induced fibroblast processes/signaling, and osteoblast-related bone remodeling and ossification.

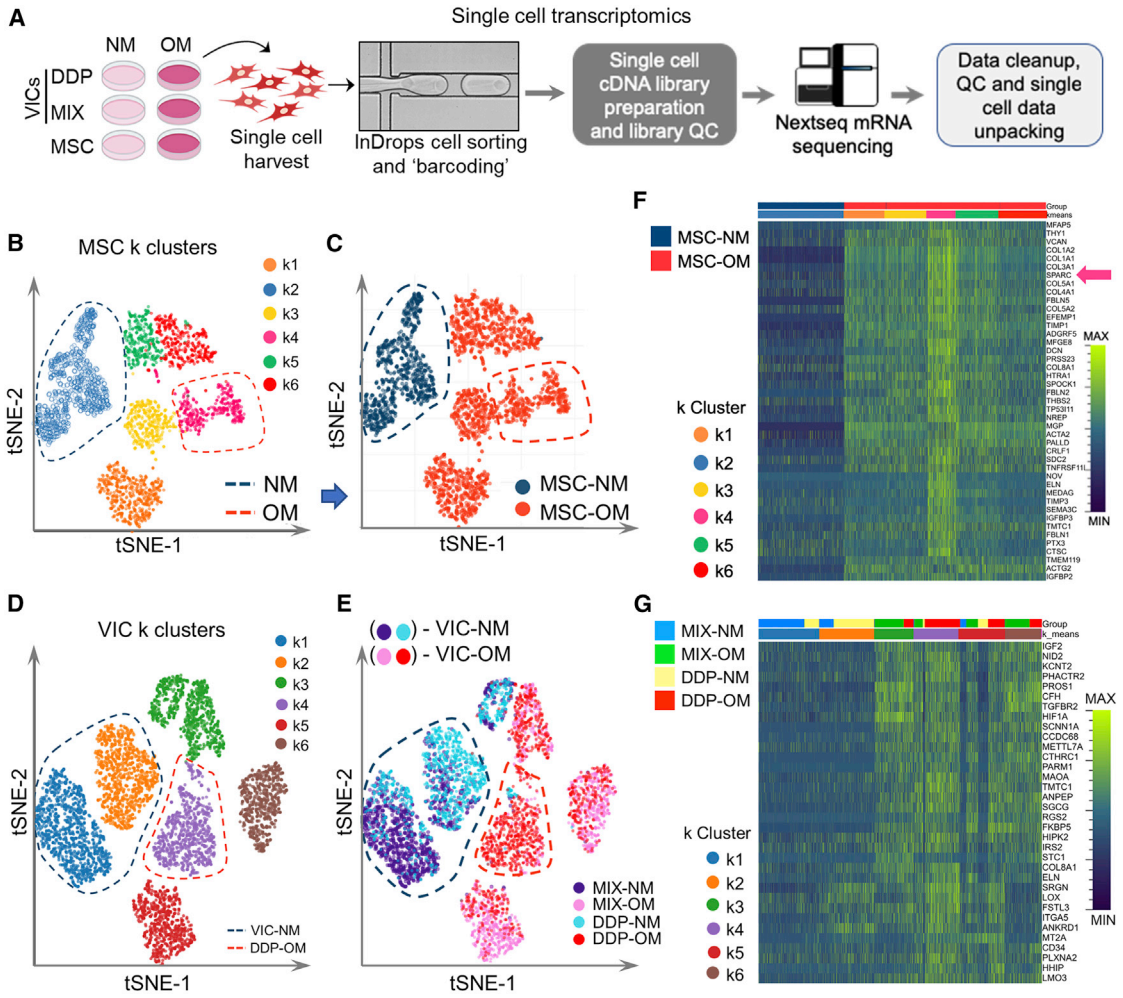

Figure 4. Single-cell RNA sequencing (scRNA-seq) of *in vitro* 2-week calcification assay with MSC-NM, MSC-OM, MIX-NM, MIX-OM, DDP-NM, and DDP-OM cells

(A) Single-cell InDrops scRNA-seq of *in vitro* calcification assay. MSCs and VICs 2-week culture in either OM or NM. Cells were detached and immediately sorted for single-cell capture, cDNA library synthesis, and sequencing.

(B) tSNE plot showing k-means clusters of MSCs.

(C) tSNE plot with MSC-NM and MSC-OM grouping.

(D) tSNE plot showing k-means clustering of VICs: VIC-NM and DDP-OM separation.

(E) tSNE plot showing k-means clusters of VICs and how MIX-NM, MIX-OM, DDP-NM, and DDP-OM separate.

(F) MSC k-clusters expression heatmap of increased DGEs from fold change $\geq$2.0 of k4 versus k2 cluster at FDR; q $\leq$ 0.05.

(G) VICs k-clusters expression heatmap of increased DEGs from fold change $\geq$1.5 of k4 versus (k1 + k2) clusters at FDR; q $\leq$ 0.05. DDP, sorted $CD44^{high}CD29^{+}CD59^{+}CD73^{+}CD45^{low}$ VICs; DEGs, differentially expressed genes; FDR, false discovery rate; MIX, mixed unsorted VICs; MSCs, mesenchymal stem cells; NM, normal media; OM, osteogenic media; QC, quality control; tSNE, t-distributed stochastic neighbors embedding; VICs, valvular interstitial cells,

.

Proteome analysis of *in vitro* modeling of aortic valve calcification

We compared the changes in the bulk proteomes of DPP-VICs and MIX-VICs during osteogenic differentiation. We performed proteomics using DDP-VICs and compared them against the MIX-VICs isolated from the same donors (n = 4). Alongside cultures of MSCs, these cell culture setups were grown in OM or NM conditions for 0, 7, 14, and 21 days (Figure 5A). Alizarin Red calcification assays demonstrate that DDP-VIC populations calcified by day 14 (resembling the calcification potential of MSCs), whereas all 4 MIX-VIC donors exhibit calcification later at day 21 (Figure 5B). Moreover, Alizarin Red staining in DDP-VICs is stronger compared to their MIX-VIC counterparts.

We analyzed the proteome during osteogenic differentiation to identify candidate drivers of calcification in each cell population (MSCs, MIX-VICs, and DDP-VICs). Proteomic analysis sequenced 3,998 proteins for the MSC-OM and MSC-NM combined and 4,538 for the MIX-VICs and DDP-VICs combined, with 3,607 (73%) proteins shared between the 2 cell types (Figure 5C).

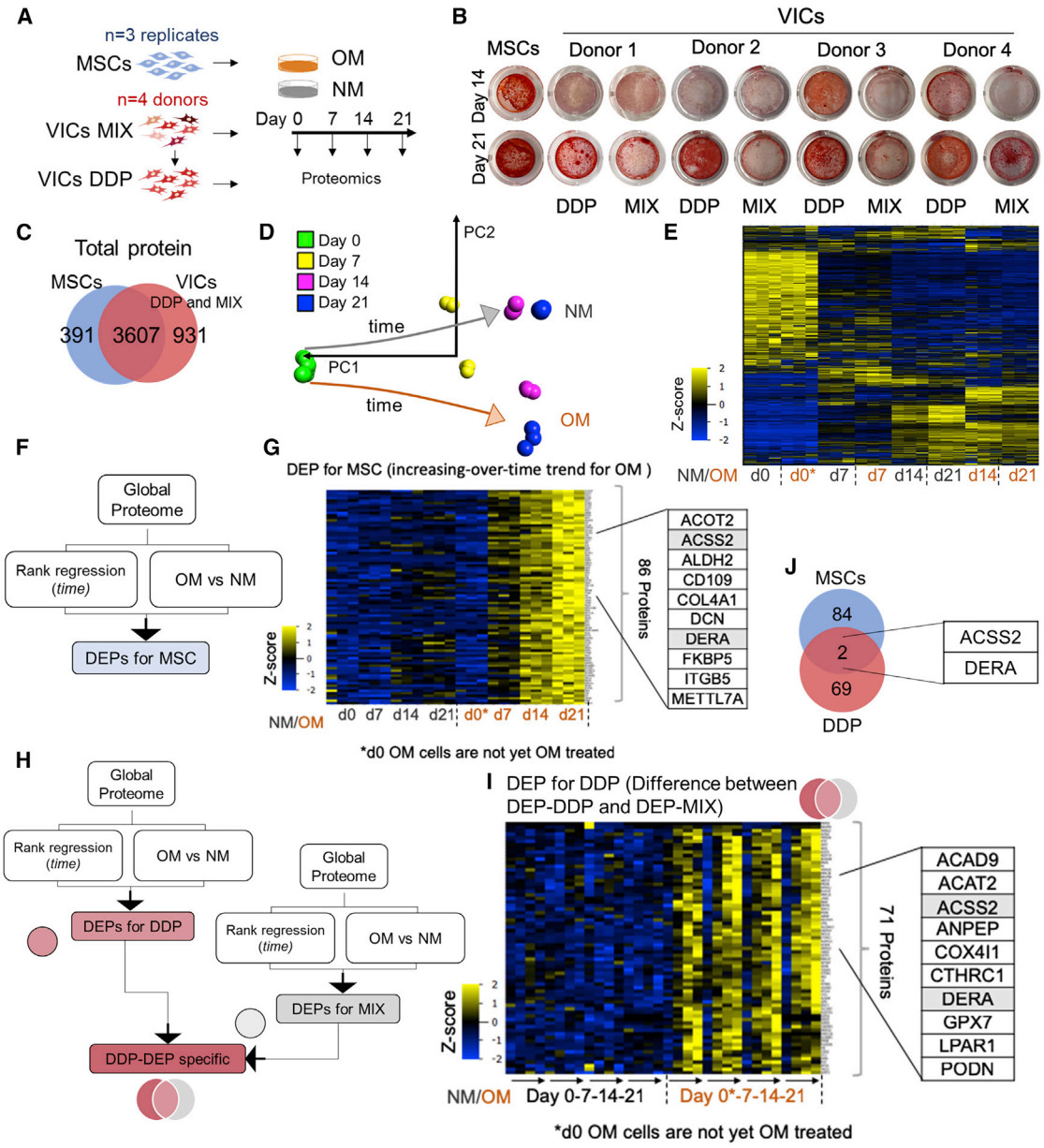

Figure 5. *In vitro* time course proteomic profiling

(A) Experimental setup of MSC, VICs MIX, and VICs DDP grown in culture using growth media, then transitioned into either OM or NM conditioned media. Time course starts from exposure, collecting proteins at different time point weekly intervals, from 0 to 3 weeks post-OM or -NM switch: days 0, 7, 14, and 21.

(B) Alizarin red calcification assay after OM treatment at 14 and 21 days, comparing MSCs with DDP and MIX (n = 4). The phenotype of DDP closely resembles MSC in OM behavior.

(C) Total proteins identified from proteomics in MSCs and VICs with a large portion of shared proteins.

(D) Principal-component analysis (PCA) of each sample condition depicting the close proximity of MSC-NM and MSC-OM at 0 weeks or immediately after switching to condition media. With increasing time points, distance between temporally paired OM and NM conditions increases in the 2D PCA space.

(E) MSC proteomics show that protein abundance difference between NM and OM are higher in the time points day 14 and day 21 than in day 0 and day 7.

(F) Analysis workflow of MSC-OM and MSC-NM proteomics data in 2 ways: a rank-regression across time points and a 2-group comparison between NM and OM. The resulting differentially expressed proteins (DEPs) were consolidated to and designated as DEPs for MSCs.

(G) DEPs in MSC-OM, increasing over time (86 proteins).

(H) Analysis workflow of VIC-MIX and VIC-DDP proteomics data. From the global proteome of either VIC-DDP or VIC-MIX, sample conditions were analyzed 2 ways: a rank-regression across time points and a 2-group comparison between media conditions. The resulting DEPs were consolidated to and designated as DEPs for VICs DDP or DEPs for VICs MIX. Further comparison of these 2 DEP lists reveals DDP-DEP-specific proteins unique to DDP not identified in MIX cells.

(I) Increasing DEPs for VICs DDP-specific proteins (71 proteins).

(J) Overlap between the DEP for MSC (86) and the DEP-DDP specific (71) with 2 shared proteins.

We compared the baseline (t_0 = day 0) proteome of the MSC-NM and MSC-OM using triplicate cell culture experiments (combined n = 6 for day 0). These replicates demonstrate that the significant source of variation is between media conditions and time points and not across sample replicates. When considering the NM and OM proteome, the PCA depicts 3 significant findings: (1) the cell culture replicates show higher proximity within each cell population versus other sample conditions; (2) there is a time progression component that (3) also drives divergence between the MSC-NM and MSC-OM samples (Figure 5D). Hierarchical cluster analysis (expression heatmap) provides an overview of the changing proteome across time and media (Figure 5E).

Multiple statistical filtering was done to (1) reduce donor-to-donor variability, (2) model the impact of time in culture, (3) identify differentially expressed proteins (DEPs) over time in both the MSC and DDP-VIC populations, and (4) model the effect of calcifying media treatment on these DEPs. The full details of our filtering approach are described in the STAR Methods and are depicted graphically in Figures 5F, 5H, S5, and S6.

The intersection of the 2 parallel filtering methods (Figures 5F and S5) resulted in 128 shared DEPs (increasing and decreasing expression) among the MSC-OM over time (Figure S5). Then, we filtered for only increasing proteins unique to MSC-OM (intersection), yielding 86 proteins (Figures 5G and S5; Table S4). To identify DDP-OM-enriched proteins, we analyzed the DDP-VIC and MIX-VIC dataset separately from and in an analogous manner to the MSC dataset (Method details) and incorporated an additional step that subtracted MIX-OM proteins from DDP-OM proteins (Figures 5H and S6), resulting in 71 proteins (Figures 5I and S6; Table S4).

CTHRC1 and MAOA are identified by DDP-VIC transcriptome and proteome and promote calcification of VICs *in vitro*

Combining scRNA-seq and *in vitro* proteomic approaches, we narrowed down our OM-mediated differential expression to 83 (scRNA-seq, 34 + 49) and 157 (proteomics, 71 + 86) candidate molecules (Figure 6A) that may be drivers of osteogenic potential in DDP-VICs and MSCs, respectively. We then aimed to determine whether these genes were shared between omics datasets and between these cell types, giving rise to shared protein lists (Figure 6A). Although none of the proteins were present in all 4 dataset gene lists, some are shared between multiple datasets or cell types, including ANPEP, NID2, CTHRC1, ACSS2, DERA, MAOA, FKBP5, METTL7A, ELN, TMTC1, COL4A1, CRFL1, and DCN. We focused on 2 proteins: (1) CTHRC1, collagen triple helix repeat-containing protein, shared in the VIC omics data (DEP and DEG lists) and the MSC-OM DEP list, and (2) MAOA, monoamine oxidase A, present in the DDP DEG and MSC-OM DEP lists. MAOA-associated high serotonin levels have been reported to cause oxidative stress in human heart valves (Pena-Silva et al., 2009). To determine whether these genes promote the calcification of VICs, we performed siRNA-mediated loss of function in OM- or NM-cultured VICs at 10 days. MAOA or CTHRC1 knockdown (silencing efficiency >90% for each gene, $p < 0.0001$; Figure 6B) results in a decreased ALPL activity (Figure 6C) and osteocalcin mRNA expression in OM-cultured VICs (n = 3) (Figure 6D). MAOA inhibitors moclobemide and pirindole demonstrated a reduction of calcification (Figure 6E). Currently, no CTHRC1 small-molecule inhibitors are available for parallel CTHRC1 testing. Immunostaining of CAVD tissue (n = 9 donors) confirmed the enrichment of MAOA and CTHRC1 expression in regions near calcifications. Non-diseased valves display negligible MAOA or CTHRC1 staining (n = 8 donors, Figure 6F). Quantification of the MAOA and CTHRC1 shows predominant expression in CAVD compared with non-diseased valves (Figures 6G and 6H). Thus, our stratified single-cell and bulk multi-omics profiling strategies (Figure 6I) were able to identify potential therapeutic targets for CAVD.

Calcification-related disease networks share common genes and pathways with the progenitor markers depicting DDP-VIC and targets identified by omics

To determine the shared molecular interactors linking MSC-OM and VIC DDP-OM multi-omics targets with calcification and DDP-VIC surface markers, we mapped their respective gene sets onto the PPI network (Method details). Increasing evidence suggests that overlapping subnetworks in the PPI network have similar functions, contain co-expressed genes, or share in disease comorbidities (Menche et al., 2015). Therefore, we aim to demonstrate the network connections within these 3 datasets and identify shared protein interactions between (1) the progenitor cell markers depicting DDP-VICs, (2) the targets detected by proteomic profiling studies, and (3) DEGs from the scRNA-seq study in association with the calcification PPI network (Figure 6J). Overall, the subnetworks made up of the genes enriched in MSC-OM and VIC DDP-OM omics data and DDP-VIC surface markers had a significant overlap in the calcification PPI network comprising calcification factors previously found to be associated with cardiovascular calcification. This new network shared 27 genes with commonly associated calcification markers (Fisher's exact test, 2-sided $p = 8.45 \times 10^{-12}$) and 7 genes with DDP surface markers (Fisher's exact test, 2-sided $p = 1.80 \times 10^{-4}$), suggesting common pathways connecting the 3 datasets. These common pathways that emerged from datasets derived from VIC profiling may be parts of a more significant underlying mechanism of CAVD and agree with currently held concepts (Schlotter et al., 2018).

DISCUSSION

Aortic VIC heterogeneity and the putative presence of a DDP in human CAVD are largely unexplored. We aimed to address this question by using human primary VICs, multiple omics, and single-cell methods in a multi-tiered workflow. We identified and comprehensively characterized a pluripotent $CD44^{high}CD29^{+}CD59^{+}CD73^{+}CD45^{low}$ VIC population and mapped it to nodes of calcification located within the disease-susceptible fibrosa layer. We showed that CAVD leaflets contain cells with an MSC-like "metakaryotic" nuclear phenotype in 3D (Gostjeva et al., 2009) and 2D systems. HTS-FC and network analysis demonstrated CD44 taking a central role in DDP-VIC regulation of calcification and was validated *in vitro*. Our results corroborate other reports on CD44 as a critical molecule in vascular calcification and VIC activation (Icer and Gezmen-Karadag, 2018). However, CD44 is ubiquitously expressed by

CellPress
OPEN ACCESS

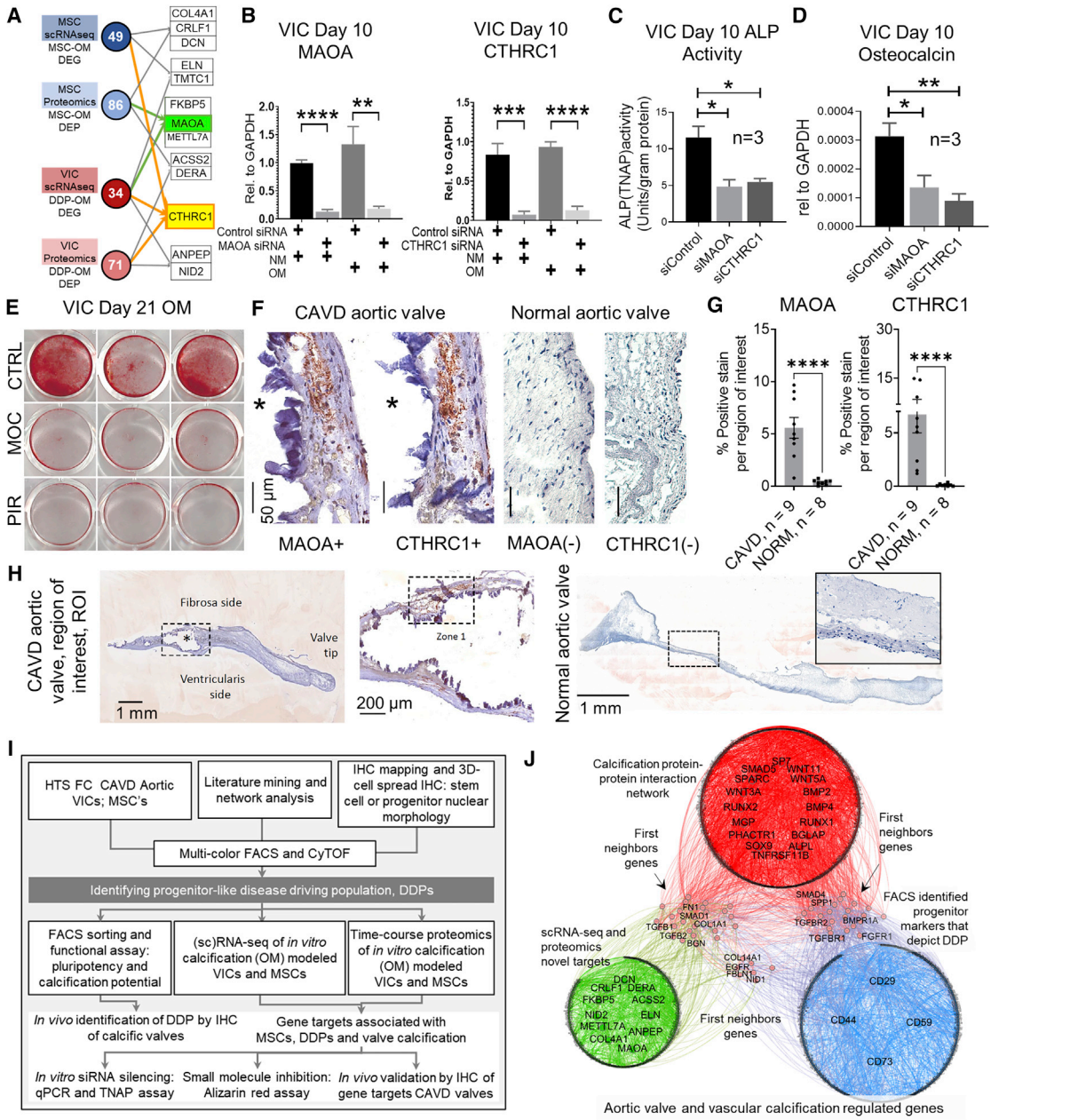

Figure 6. Target gene selection from multi-omics data

(A) A total of 13 proteins appearing ≥2 times in the increasing DEP or DEG lists from either proteomics or single-cell transcriptomics analysis among OM-conditioned MSCs and VIC-DDP cells. CTHRC1 is present in 3 increased differential expression lists. MAOA, an enzyme not commonly associated with calcification.

(B) MAOA and CTHRC1 mRNA silencing efficiency in VICs (pre-NM/OM culture) 10 days post-culture.

(C) VICs tissue nonspecific alkaline phosphatase (ALP) activity decreased in OM-treated MAOA- or CTHRC1-silenced VICs; n = 3 donors, post-10 days.

(D) Osteocalcin mRNA expression after MAOA or CTHRC1 silencing (post-10 days *in vitro*, n = 3).

(E) VICs Alizarin red staining after 21 days in OM with PBS (control), moclobemide 10 µM, or pirlindole 10 µM; n = 3).

(F) IHC of MAOA$^+$ cells and CTHRC1$^+$ cells showing close proximity to calcification areas, but not in cells distal to calcification; representative images, n = 9 donors. IHC of normal aortic valves showing sparse or negative staining for MAOA and CTHRC1; n = 8 donors.

(G) Quantification of MAOA and CTHRC1 relative expression on CAVD (n = 9) and normal valves (n = 8) using percent positive staining per tissue area of the region of interest (ROI), hue-saturation-value (HSV) method, using cellSens Dimension version 1.9 software (Olympus).

(H) Whole-valve IHC image for both CAVD and normal aortic valves, representative images, and the comparable ROIs quantified.

(I) Multi-tiered target discovery workflow starting with unbiased screening and systems biology-based prioritization identifies DDP, followed by mechanistic exploration and target gene validation.

(legend continued on next page)

various cells (Jordan et al., 2015). Hence, therapeutic targeting of CD44 may have unintended systemic effects. CD29 is recently reported as a pro-calcifying progenitor cell marker in atherosclerosis (Cho et al., 2018), while CD59 is highly associated with adipogenic and osteogenic capacities of mesenchymal stromal cells (Moravcikova et al., 2018), and CD73 is implicated in innate immunity (Kim and Hematti, 2009). Thus, they are deprioritized as potential CAVD therapeutic targets even though we acknowledge the important role of CD73 in valvular mineralization (Mahmut et al., 2015). After establishing the $CD44^{high}D29^{+}CD59^{+}CD73^{+}CD45^{low}$ phenotype as a DDP-VIC in CAVD, we explored gene expression through time course proteomics and single-cell transcriptomics, qPCR, and functional differentiation analyses by comparing valve FACS-isolated and *in vitro* expanded $CD44^{high}CD29^{+}CD59^{+}CD73^{+}CD45^{low}$ DDP-VICs against its autologous source of unsorted MIX-VICs.

In scRNA-seq, a subcluster of MSC-OM cells express various collagens (e.g., COL1A1, COL1A2, COL3A1, COL5A1, COL5A2, COL6A1) and calcification-related genes (e.g., SPARC, SPOCK1, TNFRSF11B/osteoprotegerin), signifying active fibroblastic and osteoblastic response to osteogenic stimuli (Baird et al., 2018). As this was not observed in our VICs-OM scRNA-seq data, it is unclear whether these genes could be appropriate for CAVD therapeutic consideration.

A majority of DDP-VICs that make up the scRNA-seq k4 cluster have the $CD44^{high}CD29^{+}CD59^{+}CD73^{+}CD45^{low}$ procalcific phenotype. Genes increased in DDP-VIC k4 cluster versus other VIC-OM clusters (k3, k5, and k6) include CD34, TMTC1, COL8A1, FKBP5, ANPEP, TGFBR2, PLXNA2, ELN, CTHRC1, and MAOA, among others (Table S2). MAOA, TMTC1, and COL8A1 were consistently enriched in the time course MSC-OM proteomics, while CTHRC1 and ANPEP were enriched in the VIC DDP-OM proteomics time course. Enrichment of CD34, congruent with HTS-FC data and VIC time course proteomics (DDP-OM), reflects the progenitor cell-like nature of the DDP-VICs. Increased TGFBR2 and PLXNA2 expression suggest osteoblastic potential in this subset (k4) of DDP-VICs. PLXNA2 mediates osteoblastic differentiation in bone mesenchymal progenitors via RUNX2 regulation (Oh et al., 2011), similar to TGFBR2 (Iwata et al., 2010). Other gene overlaps are COL4A1, CRLF1, and DCN, differentially enriched in both MSC-OM scRNA-seq and MSC-OM proteomics. DCN is known to retain low-density lipoprotein in valvular disease (Neufeld et al., 2014), while CRLF1 in mouse osteoblasts is speculated to be important in bone formation (Clancy et al., 2003). ACSS2, another lipid storage gene, is enriched in both VIC-DDP-OM proteomics and MSC-OM proteomics (Figure 6A). Lastly, FKBP5, a glucocorticoid pathway-binding protein present in VIC-DDP-OM proteomics, DDP-VIC scRNA-seq, and MSC-OM proteomics, has as yet unclear implications in the calcification process.

MAOA and CTHRC1 could serve as potential therapeutic anti-calcification targets based on their co-regulated induction with other calcification-related genes such as SPARC, ELN, FN1, FBN, and COL8A1. MAOA is also co-enriched with CD34, a stem cell marker, and various myofibroblast and osteoblast differentiation markers, including ELN, COL8A, ACTA2, and TGFBR2. Pathways enrichment validates this shared mechanism of osteoblast differentiation of progenitor-like cells between the VIC and the MSC scRNA-seq datasets, corroborating the role of $CD44^{high}D29^{+}CD59^{+}CD73^{+}CD45^{low}$ DDP-VICs as a disease driver in human CAVD.

MAOA has not yet been reported as a regulator in the calcification process. We demonstrated that MAOA silencing during VIC osteogenic differentiation effectively reduces calcification-related gene expression and intracellular ALP activity. CTHRC1 is implicated in CAVD through bioinformatic screening studies (Liu et al., 2017) of human aortic valve gene expression datasets. CTHRC1 also binds and activates WNT5A and WNT11 (Yamamoto et al., 2008), parts of the noncanonical WNT signaling in human CAVD (Albanese et al., 2017). CTHRC1 is present in calcifying human atherosclerotic plaques (Pyagay et al., 2005). In our study, *in vitro* CTHRC1 loss of function reduced calcification-related gene expression and ALP activity in VICs-OM conditions, thereby confirming CTHRC1 as a potential anti-calcification target.

By using single-cell analytic tools, transcriptomics and proteomics methods, and network analysis, we identify a roster of potential therapeutic candidates for human CAVD. A similar stepwise omics approach may be advantageous for therapeutic target discovery in other disease contexts.

Limitations of the study

Several limitations of this study include the lack of further definitive tests for both pluripotency and stemness of the identified VIC subpopulation. Further characterization of stem cell features, such as metabolic profiling and extensive lineage differentiation, needs to be done. There is a need for deeper exploration of the disease-driver mechanisms of this VIC population, such as procalcific vesicle biogenesis and pathophysiologic triggers for their osteogenic differentiation. Potential mechanistic marker evaluation through quantitative testing in an *in vivo* model of aortic valve calcification such as randomized loss of function or intervention trials also needs to be explored. The follow-up *in vivo* investigation and further characterization of population markers will be done as part of a sequel study.

STAR★METHODS

Detailed methods are provided in the online version of this paper and include the following:

- KEY RESOURCES TABLE
- RESOURCE AVAILABILITY
  - Lead contact

(J) Systems approach to single-cell and bulk multi-omics strategies for exploring VICs in human CAVD. PPI network connects the subnetworks of 4 DDP markers (blue, inner circle hubs) and their first neighbors (blue, outer circle nodes), sc-transcriptomics and proteomics filtered targets (green, inner circle hubs) and their first neighbors (green, outer circle nodes), and aortic valve and vascular calcification-associated markers (red, inner circle hubs) and their first neighbors (red, outer circle nodes). Subnetworks share several first-neighbor connections (salmon-colored nodes between green, red, and blue networks).
ns $p > 0.05$, *$p \leq 0.05$, **$p \leq 0.01$, ***$p \leq 0.001$, ****$p \leq 0.0001$. For (F)–(H), the asterisk indicates the calcification area. Bar graphs are means ± SEMs.

SUPPLEMENTAL INFORMATION

Supplemental information can be found online at https://doi.org/10.1016/j.celrep.2022.110685.

ACKNOWLEDGMENTS

We thank the Dana-Farber Cancer Institute (DFCI) Flow Cytometry Core and Mass Cytometry Core, John Daley II, Susan Lazo, Nicole Paul, Eric Haas, and Cory Williams for assistance with HTS FACS and CyTOF. We are grateful to the Harvard Medical School Single Cell Core: Mandovi Chaterjee, Sarah Boswell, and Alex Ratner for InDrops service, as well as Zach Herbert, Maura Berkeley, and Andrew Caruso of the DFCI Molecular Biology and Core Facilities (MBCF) for assisting us in scRNA-seq. We also thank Shannan Ho-Shui and Michael Steinbaugh of the Harvard Chan Bioinformatics Core, Harvard School of Public Health; Ian Taylor, Joel Connors, and Miguel Velasquez of FlowJo; and LLC/BD Biosciences for the data analytics support. E.A. is supported by the National Institutes of Health (NIH) grants R01HL136431, R01HL141917, and R01HL147095. M.A. is supported by NIH grants R01HL107550 and R01HL126901 and by Kowa Company, Nagoya, Japan.

AUTHOR CONTRIBUTIONS

J.L.D. and E.A. conceived the project. J.L.D. and P.V. initiated the project. J.L.D. and Y.I. designed, performed, analyzed, and interpreted the data for the majority of the experiments. J.L.D., Y.I., S.G., J.T.M., A.H., L.H.L., and B.P. contributed analytic tools, analyzed data, and performed data visualization. J.L.D., Y.I., S.G., J.Y.L., S.C., J.S.-N., F.B.-L., P.V., E.G., H.S., S.A.S., J.W., and H.H. performed the experiments. J.L.D. and Y.I. drafted the original manuscript. S.A.S., M.B., and J.Y.L. contributed to the original manuscript drafting. S.C.B. provided the aortic valve specimens. J.L.D., E.A., M.B., and S.A.S. reviewed and edited the manuscript. J.L.D. revised the manuscript. J.L.D., J.T.M., S.C., and F.B.-L. performed experiments for the revision. E.A. supervised the project and provided funds and resources.

DECLARATION OF INTERESTS

M.A. is also supported by grants from Kowa Company, Ltd., Nagoya, Japan.

INCLUSION AND DIVERSITY

One or more of the authors of this paper self-identifies as an underrepresented ethnic minority in science. While citing references scientifically relevant for this work, we also actively worked to promote gender balance in our reference list.

Received: December 17, 2020
Revised: August 4, 2021
Accepted: March 24, 2022
Published: April 12, 2022

REFERENCES

Aikawa, E., and Libby, P. (2017). A rock and a hard place: chiseling away at the multiple mechanisms of aortic stenosis. Circulation *135*, 1951–1955.

Albanese, I., Yu, B., Al-Kindi, H., Barratt, B., Ott, L., Al-Refai, M., de Varennes, B., Shum-Tim, D., Cerruti, M., Gourgas, O., et al. (2017). Role of noncanonical Wnt signaling pathway in human aortic valve calcification. Arterioscler. Thromb. Vasc. Biol. *37*, 543–552.

Baird, A., Lindsay, T., Everett, A., Iyemere, V., Paterson, Y.Z., McClellan, A., Henson, F.M.D., and Guest, D.J. (2018). Osteoblast differentiation of equine induced pluripotent stem cells. Biol. Open *7*, bio033514.

Bastian, M., Heymann, S., and Jacomy, M. (2009). Gephi : An Open Source Software for Exploring and Manipulating Networks. Third International ICWSM Conference, 361–362. https://www.aaai.org/ocs/index.php/ICWSM/09/paper/view/154.

Boyer, L.A., Lee, T.I., Cole, M.F., Johnstone, S.E., Levine, S.S., Zucker, J.P., Guenther, M.G., Kumar, R.M., Murray, H.L., Jenner, R.G., et al. (2005). Core transcriptional regulatory circuitry in human embryonic stem cells. Cell *122*, 947–956.

Chellan, B., Rojas, E., Zhang, C., and Hofmann Bowman, M.A. (2018). Enzyme-modified non-oxidized LDL (ELDL) induces human coronary artery smooth muscle cell transformation to a migratory and osteoblast-like phenotype. Sci. Rep. *8*, 11954.

Cho, H.-J., Lee, J.-W., Cho, H.-J., Lee, C.-S., and Kim, H.-S. (2018). Identification of adult mesodermal progenitor cells and hierarchy in atherosclerotic vascular calcification. Stem Cells *36*, 1075–1096.

Chu, F.-Y., Haley, S.C., and Zidovska, A. (2017). On the origin of shape fluctuations of the cell nucleus. Proc. Natl. Acad. Sci. U S A *114*, 10338.

Ciceri, P., Elli, F., Cappelletti, L., Tosi, D., Savi, F., Bulfamante, G., and Cozzolino, M. (2016). Osteonectin (SPARC) expression in vascular calcification: *in vitro* and *ex vivo* studies. Calcif. Tissue Int. *99*, 472–480.

Clancy, B.M., Johnson, J.D., Lambert, A.J., Rezvankhah, S., Wong, A., Resmini, C., Feldman, J.L., Leppanen, S., and Pittman, D.D. (2003). A gene

expression profile for endochondral bone formation: oligonucleotide microarrays establish novel connections between known genes and BMP-2-induced bone formation in mouse quadriceps. Bone *33*, 46–63.

Decano, J.L., and Aikawa, M. (2018). Dynamic macrophages: understanding mechanisms of activation as guide to therapy for atherosclerotic vascular disease. Front. Cardiovasc. Med. *5*, 97.

Decano, J.L., Singh, S.A., Gasparotto Bueno, C., Ho Lee, L., Halu, A., Chelvanambi, S., Matamalas, J.T., Zhang, H., Mlynarchik, A.K., Qiao, J., et al. (2021). Systems approach to discovery of therapeutic targets for vein graft disease: PPARα pivotally regulates metabolism, activation, and heterogeneity of macrophages and lesion development. Circulation *143*, 2454–2470.

Dimitrios, S., and Monos, R.J.W. (2018). Clinical Immunology - Principles and Practice, 5th Edition (ScienceDirect), pp. 79–92.e71.

Gostjeva, E.V., Koledova, V., Tomita-Mitchell, A., Mitchell, M., Goetsch, M.A., Varmuza, S., Fomina, J.N., Darroudi, F., and Thilly, W.G. (2009). Metakaryotic stem cell lineages in organogenesis of humans and other metazoans. Organogenesis *5*, 191–200.

Hagberg, A., Swart, P., and S Chult, D. (2008). Exploring network structure, dynamics, and function using networkx. United States. https://www.osti.gov/servlets/purl/960616.

Hinton, R.B., Lincoln, J., Deutsch, G.H., Osinska, H., Manning, P.B., Benson, D.W., and Yutzey, K.E. (2006). Extracellular matrix remodeling and organization in developing and diseased aortic valves. Circ. Res. *98*, 1431–1438.

Icer, M.A., and Gezmen-Karadag, M. (2018). The multiple functions and mechanisms of osteopontin. Clin. Biochem. *59*, 17–24.

Iung, B., Baron, G., Butchart, E.G., Delahaye, F., Gohlke-Barwolf, C., Levang, O.W., Tornos, P., Vanoverschelde, J.L., Vermeer, F., Boersma, E., et al. (2003). A prospective survey of patients with valvular heart disease in Europe: the Euro heart survey on valvular heart disease. Eur. Heart J. *24*, 1231–1243.

Iwata, J.-I., Hosokawa, R., Sanchez-Lara, P.A., Urata, M., Slavkin, H., and Chai, Y. (2010). Transforming growth factor-β regulates basal transcriptional regulatory machinery to control cell proliferation and differentiation in cranial neural crest-derived osteoprogenitor cells. J. Biol. Chem. *285*, 4975–4982.

Jevtić, P., Edens, L.J., Vuković, L.D., and Levy, D.L. (2014). Sizing and shaping the nucleus: mechanisms and significance. Curr. Opin. Cell Biol. *28*, 16–27.

Jordan, A.R., Racine, R.R., Hennig, M.J.P., and Lokeshwar, V.B. (2015). The Role of CD44 in disease pathophysiology and targeted treatment. Front. Immunol. *6*, 182.

Kim, J., and Hematti, P. (2009). Mesenchymal stem cell–educated macrophages: a novel type of alternatively activated macrophages. Exp. Hematol. *37*, 1445–1453.

Liu, M., Luo, M., Sun, H., Ni, B., and Shao, Y. (2017). Integrated bioinformatics analysis predicts the key genes involved in aortic valve calcification: from hemodynamic changes to extracellular remodeling. Tohoku J. Exp. Med. *243*, 263–273.

Mahmut, A., Boulanger, M.-C., Bouchareb, R., Hadji, F., and Mathieu, P. (2015). Adenosine derived from ecto-nucleotidases in calcific aortic valve disease promotes mineralization through A2a adenosine receptor. Cardiovasc. Res. *106*, 109–120.

Mason, D.Y., and Gatter, K.C. (1987). The role of immunocytochemistry in diagnostic pathology. J. Clin. Pathol. *40*, 1042.

McQuin, C., Goodman, A., Chernyshev, V., Kamentsky, L., Cimini, B.A., Karhohs, K.W., Doan, M., Ding, L., Rafelski, S.M., Thirstrup, D., et al. (2018). CellProfiler 3.0: next-generation image processing for biology. PLoS Biol. *16*, e2005970.

McQuin, C., Goodman, A., Chernyshev, V., Kamentsky, L., Cimini, B.A., Karhohs, K.W., Doan, M., Ding, L., Rafelski, S.M., Thirstrup, D., et al. (2018). CellProfiler 3.0: Next-generation image processing for biology. PLOS Biology *16*, e2005970.

Menche, J., Sharma, A., Kitsak, M., Ghiassian, S.D., Vidal, M., Loscalzo, J., and Barabási, A.-L. (2015). Uncovering disease-disease relationships through the incomplete interactome. Science *347*, 1257601.

Millar, S.A., Patel, H., Anderson, S.I., England, T.J., and O'Sullivan, S.E. (2017). Osteocalcin, vascular calcification, and atherosclerosis: a systematic review and meta-analysis. Front. Endocrinol. *8*, 183.

Moravcikova, E., Meyer, E.M., Corselli, M., Donnenberg, V.S., and Donnenberg, A.D. (2018). Proteomic profiling of native unpassaged and culture-expanded mesenchymal stromal cells (MSC). Cytometry A *93*, 894–904.

Neufeld, E.B., Zadrozny, L.M., Phillips, D., Aponte, A., Yu, Z.X., and Balaban, R.S. (2014). Decorin and biglycan retain LDL in disease-prone valvular and aortic subendothelial intimal matrix. Atherosclerosis *233*, 113–121.

Nishimura, I., Hisanaga, R., Sato, T., Arano, T., Nomoto, S., Ikada, Y., and Yoshinari, M. (2015). Effect of osteogenic differentiation medium on proliferation and differentiation of human mesenchymal stem cells in three-dimensional culture with radial flow bioreactor. Regen. Ther. *2*, 24–31.

Nomura, A., Seya, K., Yu, Z., Daitoku, K., Motomura, S., Murakami, M., Fukuda, I., and Furukawa, K.-I. (2013). CD34-negative mesenchymal stem-like cells may act as the cellular origin of human aortic valve calcification. Biochem. Biophys. Res. Commun. *440*, 780–785.

Oh, J.-E., Kim, H.J., Kim, W.-S., Lee, Z.H., Ryoo, H.-M., Hwang, S.J., Lee, Y., and Kim, H.-H. (2011). PlexinA2 mediates osteoblast differentiation via regulation of Runx2. J. Bone Mineral Res. *27*, 552–562.

Oliveros, J. (2007). Venny. An interactive tool for comparing lists with Venn diagrams. http://bioinfogp.cnb.csic.es/tools/Venny/index.html.

Pajerowski, J.D., Dahl, K.N., Zhong, F.L., Sammak, P.J., and Discher, D.E. (2007). Physical plasticity of the nucleus in stem cell differentiation. Proc. Natl. Acad. Sci. *104*, 15619.

Pena-Silva, R.A., Miller, J.D., Chu, Y., and Heistad, D.D. (2009). Serotonin produces monoamine oxidase-dependent oxidative stress in human heart valves. Am. J. Physiol. Heart Circ. Physiol. *297*, H1354–H1360.

Perez-Riverol, Y., Csordas, A., Bai, J., Bernal-Llinares, M., Hewapathirana, S., Kundu, D.J., Inuganti, A., Griss, J., Mayer, G., Eisenacher, M., et al. (2019). The PRIDE database and related tools and resources in 2019: improving support for quantification data. Nucleic Acids Res. *47*, D442–D450.

Pyagay, P., Heroult, M., Wang, Q., Lehnert, W., Belden, J., Liaw, L., Friesel, R.E., and Lindner, V. (2005). Collagen triple helix repeat containing 1, a novel secreted protein in injured and diseased arteries, inhibits collagen expression and promotes cell migration. Circ. Res. *96*, 261–268.

Qiu, P. (2017). Toward deterministic and semi-automated SPADE analysis. Cytometry A *91*, 281–289.

Rabkin, E., Aikawa, M., Stone James, R., Fukumoto, Y., Libby, P., and Schoen Frederick, J. (2001). Activated interstitial myofibroblasts express catabolic enzymes and mediate matrix remodeling in myxomatous heart valves. Circulation *104*, 2525–2532.

Schlotter, F., Halu, A., Goto, S., Blaser, M.C., Body, S.C., Lee, L.H., Higashi, H., DeLaughter, D.M., Hutcheson, J.D., Vyas, P., et al. (2018). Spatiotemporal multi-omics mapping generates a molecular atlas of the aortic valve and reveals networks driving disease. Circulation *138*, 377–393.

Shannon, P., Markiel, A., Ozier, O., Baliga, N.S., Wang, J.T., Ramage, D., Amin, N., Schwikowski, B., and Ideker, T. (2003). Cytoscape: a software environment for integrated models of biomolecular interaction networks. Genome Res. *13*, 2498–2504.

Stone, H.J., and Willis, M.S. (2014). In Cellular and Molecular Pathobiology of Cardiovascular Disease (Calcific and Degenerative Heart Valve Disease), E. Aikawa and F.J. Schoen, eds. (Elsevier), pp. 161–168.

Walmsley, G.G., Atashroo, D.A., Maan, Z.N., Hu, M.S., Zielins, E.R., Tsai, J.M., Duscher, D., Paik, K., Tevlin, R., Marecic, O., et al. (2015). High-throughput screening of surface marker expression on undifferentiated and differentiated human adipose-derived stromal cells. Tissue Eng. Part A *21*, 2281–2291.

Yamamoto, S., Nishimura, O., Misaki, K., Nishita, M., Minami, Y., Yonemura, S., Tarui, H., and Sasaki, H. (2008). Cthrc1 selectively activates the planar cell polarity pathway of wnt signaling by stabilizing the Wnt-receptor complex. Dev. Cell *15*, 23–36.

Yu, P., Nguyen, B.T., Tao, M., Campagna, C., and Ozaki, C.K. (2010). Rationale and practical techniques for mouse models of early vein graft adaptations. J. Vasc. Surg. *52*, 444–452.

Ziegenhain, C., Vieth, B., Parekh, S., Reinius, B., Guillaumet-Adkins, A., Smets, M., Leonhardt, H., Heyn, H., Hellmann, I., and Enard, W. (2017). Comparative analysis of single-cell RNA sequencing methods. Mol. Cell *65*, 631–643.e634.

Zilionis, R., Nainys, J., Veres, A., Savova, V., Zemmour, D., Klein, A.M., and Mazutis, L. (2017). Single-cell barcoding and sequencing using droplet microfluidics. Nat. Protoc. *12*, 44–73.

STAR★METHODS

KEY RESOURCES TABLE

REAGENT or RESOURCE	SOURCE	IDENTIFIER
Antibodies		
Donkey anti-Rabbit IgG (H + L) Highly Cross-Adsorbed Secondary Antibody, Alexa Fluor 488	Thermo Fisher	A-21206; RRID: AB_2535792
Goat anti-mouse IgG AF488	Invitrogen	A11017; RRID: AB_143160
Anti-α-SMA Cy3	Sigma	C6198; RRID: AB_476856
Anti-human CD44 PE	eBiosciences	12-0441-83; RRID: AB_465665
Anti-human CD44 (IM7 clone) APC Cy7	Biolegend	103027; RRID: AB_830784
Anti-human CD44, unconjugated	Abcam	ab157107; RRID: AB_2847859
Anti-human CD29, Alexa Fluor 488	Biolegend	303015; RRID: AB_493026
Anti-human CD29, APC	Biolegend	303007; RRID: AB_314323
Anti-human CD29, unconjugated	Abcam	ab134179; RRID: not found
Anti-human CD59, PE	Biolegend	304707; RRID: AB_2275871
Anti-human CD73, PE Cy7	BD Biosciences	344009; RRID: AB_2561541
Anti-human CD73, unconjugated	GeneTex	GTX54475; RRID: not found
Anti-human CD45, Alexa Fluor 467	Biolegend	393405; RRID: AB_2750082
Anti-human CD45, unconjugated	GeneTex	GTX28216; RRID: AB_368339
Anti-human NANOG, unconjugated	Biolegend	674202; RRID: AB_2564574
Anti-human Osteocalcin, unconjugated	Abcam	ab93876; RRID: AB_10675660
Anti-human CD90, unconjugated	Abcam	ab23894; RRID: AB_447748
Anti-human CD90, PE Cy7	Biolegend	328124; RRID: AB_2561693
Anti-human CD90, PE	Biolegend	328109; RRID: AB_893442
Anti-human CD34, unconjugated	Abcam	Ab81289; RRID: AB_1640331
Anti-human CD34, AF488	Biolegend	343517; RRID: AB_1937204
Anti-human CD34, APC	Biolegend	343607; RRID: AB_2074356
Anti-human Vimentin, unconjugated	Abcam	Ab92547; RRID: AB_10562134
Anti-human Vimentin, PE	Life Technologies	MA1-19656; RRID: AB_1088253
Anti-human Vimentin, APC	R&D	IC2105A; RRID: not found
Anti-human CD133, unconjugated	Genetex	GTX60471; RRID: AB_2887971
Anti-human CD133, Alexa Fluor 488	EMD Millipore Inc.	MAB4310X; RRID: AB_2268790
Anti-human CD146, unconjugated	Biolegend	361015; RRID: AB_2564359
Anti-human CD105, unconjugated	Abcam	ab107595; RRID: AB_10863525
Anti-human c-kit, unconjugated	Cell Signaling Technologies	3308S; RRID: AB_659956
Anti-human Ki67, unconjugated	Abcam	ab8191; RRID: AB_306346
Anti-human Ki67, APC	Biolegend	350513; RID: AB_10959326
Anti-human CD13, PE	Biolegend	301703; RRID: AB_314179
Anti-human CD55, PE	Biolegend	311308; RRID: AB_314865
141Pr-Anti-human CD45	Fluidigm	3141009B; RRID: not found
143Nd-Anti-human GFAP	Fluidigm	3143022B; RRID: not found
146Nd-Anti-human VE-Cad	HMS Lederer Core facility	N/A; RRID: not found
149Sm-Anti-human CD34	Fluidigm	3149013B; RRID: AB_2756285
150Nd-Anti-human CD63	Fluidigm	3150021B; RRID: not found
154Sm-Anti-human Vimentin	Fluidigm	3154014A; RRID: not found
155Gd-Anti-human ALPL (TNAP)	HMS Lederer Core facility	N/A; RRID: not found
156Gd-Anti-human CD29	Fluidigm	3156007B; RRID: not found

(*Continued on next page*)

Continued

REAGENT or RESOURCE	SOURCE	IDENTIFIER
159Tb-Anti-human NANOG	HMS Lederer Core facility	N/A; RRID: not found
162Dy-Anti-human ki-67	Fluidigm	3162012B; RRID: not found
163Dy-Anti-human TGFβ	Fluidigm	3163010B; RRID: AB_2888928
166Er-Anti-human CD44	Fluidigm	3166001B; RRID: AB_2744692
168Er-Anti-human CD73	Fluidigm	3168015B; RRID: AB_2810249
169Tm-Anti-human aSMA	HMS Lederer Core facility	N/A; RRID: not found
170Er-Anti-human CD105	HMS Lederer Core facility	N/A; RRID: not found
172Yb-Anti-human pS6	Fluidigm	3172008A; RRID: not found
173Yb-Anti-human CD59	Fluidigm	3173009B; RRID: not found
174Lu-Anti-human OCN	HMS Lederer Core facility	N/A; RRID: not found
176Yb-Anti-human Sortilin	HMS Lederer Core facility	N/A; RRID: not found
Donkey anti-goat IgG AF594	Thermo Fisher	A-11058; RRID: AB_2534105
Bacterial and virus strains		
No bacterial or virus strains used	N/A	N/A; RRID: not found
Biological samples		
Human CAVD post-operative aortic valve leaflets	BWH	N/A
Human Normal aortic valve leaflets, post-autopsy	BWH	N/A
HAoVIC, Normal valve leaflets cells from human donor # 1	Lonza	CBS-58004A; RRID: not found
hVIC, Normal valve leaflets cells from human donor # 2	Lonza	00225974; RRID: not found
Chemicals, peptides, and recombinant proteins		
Formalin	Thermo Fisher Scientific	SF96-20
Picrosirius red solution	VWR	KT037
Picric acid		N/A
SHUR/Mount™ Liquid Mounting Medium, TBS®	VWR	15148-062
VECTASHIELD® Antifade Mounting Medium with DAPI	Vector Laboratories	H-1200; RRID: AB_2336790
Harris Modified Method Hematoxylin Stains	Thermo Fisher Scientific	SH30-4D; SH30-500D
Eosin Y 1%	VWR	10143-130
Radioimmunoprecipitation assay buffer (RIPA) buffer	Cell Signaling Technologies	9806
Protease inhibitor cocktail	Sigma Aldrich	P8340-5ML
Chloroform(Approx. 0.75% Ethanol as Preservative/Molecular Biology),	Thermo Fisher Scientific	BP1145-1
Methanol, Optima™ LC/MS Grade, Fisher Chemical	Thermo Fisher Scientific	A456-1
Urea	Sigma Aldrich	U4884-500G
Thiourea ReagentPlus®, ≥99.0%	Sigma Aldrich	T7875-500G
UltraPure™ 1M Tris-HCl, pH 8.0	Thermo Fisher Scientific	15568025
Triethylammonium bicarbonate	Sigma Aldrich	17902-100ML
RapiGest SF	Waters Technologies Corporation	186001861
Tris(2-carboxyethyl)-phosphine hydrochloride	Sigma -Aldrich	77720
Iodoacetamide	Thermo Fisher Scientific	A39271
Lysyl Endopeptidase	Fujifilm Wako	125-05061
Fisher chemical Water, Optima™ LC/MSGrade	Thermo Fisher Scientific	W6-1
Trifluoroacetic acid for HPLC, ≥99.0%	Sigma-Aldrich	302031-10X1ML
OASIS® HLB extraction cartridge	Waters Technologies Corporation	186000383
Acetonitrile	Thermo Fisher Scientific	A955-1

(*Continued on next page*)

Continued

REAGENT or RESOURCE	SOURCE	IDENTIFIER
Formic Acid	Thermo Fisher Scientific	28905
Dimethyl sulfoxide, DMSO, molecular biology grade	Sigma-Aldrich	D8418-100ML
Isotonic sodium chloride solution	Mountainside Medical Equipment	H04888-10
Dulbecco's modified eagle's medium	Thermo Fisher Scientific	10569010
Fetal calf serum	Thermo Fisher Scientific	97068-085
Penicillin and streptomycin	VWR	45000-652
PerfeCTa® qPCR SuperMix	VWR	95050-100
Lipofectamine RNAiMAX	Invitrogen	13778075
β-glycerophosphate	EMD Millipore	35675-50GM
Dexamethasone	Fisher Scientific	ICN19456125
ascorbic acid	Sigma –Aldrich	A4544-25G
Insulin-Transferrin-Selenium-Ethanolamine (ITS+)	Thermo Fisher Scientific	51500056
2-phospho-L-ascorbic-acid	Thermo Fisher Scientific	49752-10G
TGF-β1	R & D Systems	100-B-001/CF
human insulin solution	Sigma Aldrich	I-9278
3-isobutyl-1-methylxanthine, IBMX	Sigma Aldrich	I5879
Indomethacin	Sigma Aldrich	I7378-5G
PeproGrow™ hMSC Mesenchymal Stem Cell Media	ATCC	XF-HMSC-500
collagenase IA-S	Sigma Aldrich	C5894-50MG
HEPES buffer	Thermo Fisher Scientific	15630-080
100 μm cell strainer	Thermo Fisher Scientific	22-363-549
OCT compound	Ager Scientific	AGR1180
Superfrost Plus Microslide glass slides	VWR	48311-703
Paraformaldehyde	Sigma Aldrich	P6148-500g
hydrogen peroxide	VWR	EM-HX0635-2
AEC solution	Agilent Technologies	K346430-2
Omnyx VL4 scanner	GE HealthCare	N/A
eBioscience Fix and Perm set	eBioscience	88-8824-00
Hoechst 33,543	BD Biosciences	561908
FluoroBrite DMEM	Thermo Fischer Scientific	A1896701
Cell-IDTM Cisplatin	Fluidigm	201064
MaxPar® cell staining buffer	Fluidigm	201068
Fix I buffer	Fluidigm	201065
Human Fc Block	BD Biosciences	564219
Alizarin red	Thermo Fisher Scientific	CM-0058
Alcian blue	Vector Laboratories	H-3501
Oil red O	Abcam	ab150678
Moclobemide	Sigma Aldrich	M3071-10MG
Pirlindole	Tocris Bioscience	0724
Accutase Cell detachment solution	BD Biosciences	561527
Critical commercial assays		
TNAP assay	Biovision	K412-500
BD Bioscience Lyoplate Human Cell Surface Marker Screening Panel	BD Biosciences	560747; RRID: AB_1953343
Pierce™ BCA Protein Assay Kit	Thermo Fisher Scientific	23225

(*Continued on next page*)

Continued

REAGENT or RESOURCE	SOURCE	IDENTIFIER
Deposited data		
Raw data, scRNAseq (MSC and VICs)	This paper	GEO Accession number: GSE194180
MSC and VICs Time course proteomics (NM vs. OM), mass spectrometry	This paper	PRIDE Accession number: PXD029949
Experimental models: Cell lines		
Adipose stroma-derived mesenchymal stem cells (MSCs)	ATCC	ATCC® PCS-500-011™, LOT# 80622175
Primary Dermal Fibroblast; Normal, Human, Adult (HDFa)	ATCC	ATCC® PCS-201-012
Oligonucleotides		
Silencer Select siRNA, Human MAOA (Assay ID s532873)	Thermo Fisher Scientific	4392420
Silencer Select siRNA, Human CTHRC1 (Assay ID s41892)	Thermo Fisher Scientific	4392420
Silencer Select Negative Control No.1 siRNA	Thermo Fisher Scientific	4390843
TaqMan® Gene Expression BMP2, Hs00154192_m1	ThermoFisher	N/A
TaqMan® Gene Expression RUNX2, Hs01047973_m1	ThermoFisher	4331182
TaqMan® Gene Expression MGP, Hs00969490_m1	ThermoFisher	4331182
TaqMan® Gene Expression ASPN, Hs01550901_m1	ThermoFisher	4331182
TaqMan® Gene Expression TNAP, Hs01029144_m1	ThermoFisher	4331182
TaqMan® Gene Expression TGFBR2, Hs00234253_m1	ThermoFisher	4331182
TaqMan® Gene Expression MAOA, Hs00165140_m1	ThermoFisher	4453320
TaqMan® Gene Expression CTHRC1, Hs00298917_m1	ThermoFisher	4448892
TaqMan® Gene Expression OCN, Hs01587813_g1	ThermoFisher	4331182
TaqMan® Gene Expression GAPDH, Hs02786624_g1	ThermoFisher	4331182
Software and algorithms		
Qlucore Omics Explorer	Qlucore	https://qlucore.com/
MetaCore	Clarivate	https://portal.genego.com/
Prism	GraphPad	https://www.graphpad.com/scientific-software/prism/
Gephi	Bastian et al., 2009	https://gephi.org/
Cytoscape	Shannon et al., 2003	https://cytoscape.org/download.html
Networkx	Hagberg et al., 2008	https://networkx.github.io/
R	www.cran.r-project.org	www.cran.r-project.org
Cytobank Premium	Cytobank/Beckman coulter	https://premium.cytobank.org/cytobank/
Venny 2.1	Oliveros, 2007	http://bioinfogp.cnb.csic.es/tools/venny/index.html
Elements software version 3.20	Nikon	MQS42570
Laplacian-of-Gaussian method	http://scikit-image.org/docs/dev/api/skimage.feature.html#id55	http://scikit-image.org/docs/dev/api/skimage.feature.html#id55
CellProfiler	McQuin et al., 2018	https://cellprofiler.org/

(*Continued on next page*)

Continued

REAGENT or RESOURCE	SOURCE	IDENTIFIER
cellSens Dimensions	Olympus	=https://www.olympus-lifescience.com/en/software/cellsens/#!cms[focus]=cmsContent6017
FlowJo	FlowJo	https://www.flowjo.com/learn/flowjo-university/flowjo
SeqGeq	FlowJo	https://www.flowjo.com/learn/flowjo-university/seqgeq
SeqGeq plugins	FlowJo Exchange	http://exchange.flowjo.com
Plotly Dashboard	Plotly	https://plotly.com/dash/
Proteome Discoverer	ThermoFisher Scientific	OPTON-30810

RESOURCE AVAILABILITY

Lead contact

Further information and requests for resources and reagents should be directed to and will be fulfilled by the lead contact Elena Aikawa (eaikawa@bwh.harvard.edu).

Materials availability

This study did not generate new unique reagents.

Data and code availability

- The proteomics data have been deposited at the ProteomeXchange Consortium via the PRIDE (Perez-Riverol et al., 2019) partner repository and are publicly available as of the date of publication. The single-cell RNA-seq data have been deposited at the GEO and are publicly available as of the date of publication. Accession numbers are listed in the Key resources table.
- This paper does not report any original code.
- Any additional information required to reanalyze the data reported in this paper is available from the Lead contact upon request.

EXPERIMENTAL MODEL AND SUBJECT DETAILS

To identify subpopulations of valvular interstitial cells (VICs) and their involvement in the origin of human calcific aortic valve disease (CAVD), we analyzed aortic valve leaflets obtained during aortic valve replacement surgical procedures on patients with CAVD. All patients provided written consent, and the study protocol for collecting human samples was approved by the Institutional Review Board and the Human Research Committee of Brigham and Women's Hospital (Brigham and Women's Hospital (BWH) approved IRB protocol: 2011P001703). Normal valves from autopsy sources (for histology) have no age or sex information because they are taken from a study with BWH IRB protocol: 2014P001505, which does not include approval for collecting demographic, clinical, or identifiable information from deceased tissue donors. This study used a total of 40 human aortic valves (post-surgery) composed of 27 male and 13 female patients with a mean age of 67 ± 9 years old. Details of the donor characteristics are included in the supplemental items as Table S5.

The adipose stoma-derived mesenchymal stem cell line (ATCC®, Cat# PCS-500-01, LOT# 80622175, was cultured and propagated up to the fourth passage prior to assay using PeproGrow™ hMSC Mesenchymal Stem Cell Media (Peprotech, Cat# XF-HMSC-500). The human normal dermal fibroblast cell line (ATCC, Cat# PCS-201-012) was propagated up to the fourth passage prior to assay using the ATCC fibroblast basal media (ATCC, Cat# PCS-201-030) supplemented with fibroblast growth kit low serum (ATCC, Cat# PCS-201-041) as per manufacturer's recommendations.

METHOD DETAILS

Cell culture maintenance

Culture media used for *in vitro* experiments are: (1) serum-free media is Dulbecco's modified Eagle's medium, DMEM (11965-092, ThermoFisher Scientific) with 1% penicillin/streptomycin (P/S) (2) normal media (NM) is DMEM with 5% of fetal bovine serum, FBS (10082147, ThermoFisher Scientific). (3) growth media (GM) is DMEM with 10% FBS. Osteogenic media (OM) was prepared using 10 mM β-glycerophosphate (35675-50GM, EMD Millipore), 0.01 mM dexamethasone (ICN19456125, Fisher Scientific) and 0.05 mg/mL ascorbic acid (A4544-25G, Sigma –Aldrich) in NM. Chondrogenic media was prepared using 0.1 μM dexamethasone, 1x Insulin-Transferrin-Selenium-Ethanolamine (ITS+) (51500056, Thermo Fisher Scientific)), 1 mM of 2-phospho-L-ascorbic-acid

(49752-10G, Sigma-Aldrich), 1 mM of L-proline (P5607-25G, Sigma-Aldrich), and 0.1% of TGF-β1 (100-B-001/CF, R&D) in serum-free NM. The complete formulation of ITS+ is: insulin 1000.0 mg/L, transferrin 550.0 mg/L, sodium selenite 0.67 mg/L, and ethanolamine 200.0 mg/L. Adipogenic media contains 1 μM dexamethasone, 0.125% of human insulin solution (I-9278, Sigma-Aldrich), 0.5 mM 3-isobutyl-1-methylxanthine, IBMX (I5879, Sigma-Aldrich), and 60 μM of indomethacin was added to NM. For the initial growth of adipose tissue-derived human MSC cell lines (ATCC), PeproGrow^{TM} hMSC Mesenchymal Stem Cell Media (Peprotech) was used. For all washing steps, if not indicated otherwise, autoclaved phosphate buffer saline (PBS, made from Lonza PBS (10X) without calcium or magnesium - Lonza Cat # 17-517Q) was used.

Isolation of aortic VICs

A 1 to 5 mm thick leaflet tissue containing contiguous parts from the leaflet base to tip, including calcified nodules, was obtained from each donor valve leaflet for histology prior to processing for enzymatic digestion. Processing the aortic valve tissue required manually removing large calcific nodules ($\sim \geq$ 2 mm diameter) from the tissue using fine forceps and mincing the tissue into $\leq$ 1mm^3 pieces. Prior to mincing, if the specimen was going to be processed downstream for mass cytometry (CyTOF), we cut valves into halves with one half containing all the visible calcific nodules, designated as the ''calcified'' sample of the valve, and one half visibly calcification-free, designated as the ''non-calcified'' sample. For specimens undergoing *in vitro* culturing for further experiments: FACS sorting, high-throughput surface markers flow cytometry screening, and multi-color flow cytometry, we minced valves without separating calcified and non-calcified portions. VICs were released from the minced tissue by enzymatic digestion in 37^{O}C using ~6 mL sterile-filtered solution of 1 mg/mL collagenase IA-S (Sigma, C5894-50MG) prepared in DMEM with 10 mM HEPES buffer (ThermoFisher, 15630-080) and 1% penicillin/streptomycin supplementation (VWR, 45000-652) for one hour with inverted mixing every 20 min. The content was then vortexed, and after the pieces had settled, the media was aspirated. After another washing step with basal media DMEM, we added a newly filtered collagenase solution to the tissue and incubated it for another 3 hours. Enzymatic digestion was stopped using ~600 μL of 100% FBS. The cell suspension was then filtered through a 100 μm cell strainer (BD Biosciences), washed, and cultured into 6 cm or 10 cm diameter Petri dishes or resuspended in 3% FBS in DMEM with 1.0 mM HEPES for downstream flow cytometry or CyTOF experiments.

Immunohistochemistry (IHC) of aortic valves

We conducted quantitative immunohistochemistry of cryosections through the aortic valve leaflet (n = 10). Frozen samples in the OCT compound (Ager Scientific, AGR1180) were cut consecutively into 6 μm thick histological sections and mounted on Superfrost Plus Microslide glass slides (VWR, Cat# 48311-703). After fixation (4% paraformaldehyde, PFA, Sigma, Cat# P6148-500g), peroxidase blocking (0.3% hydrogen peroxide, VWR, Cat# EM-HX0635-2), and serum blocking (4% fetal calf serum, VWR, Cat# 10158-358, Lot# 147A15), sections were incubated with primary antibodies (Antibody supplementary table) associated with calcification, VICs or mesenchymal stem cell (MSC) properties. After 1.5 hours of incubation and an additional washing step, we incubated the sections in a biotin-labeled secondary antibody at a concentration of 1:100, followed by a streptavidin-peroxidase treatment and an AEC solution (Agilent Technologies, Cat# K346430-2) incubation to achieve color development. After a quick counterstain with Harris-hematoxylin (VWR, Cat# K346430-2), we examined the slides using an Omnyx VL4 scanner (GE Healthcare) then processed them with the Elements software version 3.20 (Nikon).

Measuring staining positivity over three layers in IHC using python sci-kit

For ten aortic valve leaflets, unbiased cell counting, and quantification of positive immunostaining signals per cell, the following markers listed in Figure 1 were done using sci-kit-image for image processing (Python). Images scanned from the Omnyx VL4 scanner (GE Healthcare) were exported at full resolution (highest resolution at 40x or 0.019 micrometer/pixel) and were then exported as a large scan of the whole valve (11,508 x 3273 pixels^2) (Figure S1A). The large image scan was split into manageable sizes (~2300 x 1600 pixels) (Figure S1B). Each split image was processed for color deconvolution to distinguish the blue hematoxylin staining against the brown DAB staining. Then, image colors were inverted so that signal stains (nuclear and IHC markers) could appear bright against the dark background (negative staining stroma) (Figure S1C). Because calcification areas and crystals stain similarly with the hematoxylin as the nuclei (Figure S1D), calcification nodules were excluded from the analysis by thresholding each object/particle identified by the algorithm using the object's largest diameters from blob sampling. For example, if the hematoxylin staining blobs are detected in close apposition (adjacent) with each other, the diameters are cumulatively summated and, as a result, will then exceed the threshold diameter in micrometers. None of the correct cell nuclei, which are each separated from other adjacent cell nuclei by non-hematoxylin staining cytoplasm, exceed ~20 micrometers, and none of the calcification nodules staining with hematoxylin are smaller than 50 micrometers. Hence, by thresholding blob diameters, calcification areas can be excluded (Figure S1E). After calcification exclusion, we again used blob detection to identify the nucleus of each cell using the Laplacian-of-Gaussian method (http://scikit-image.org/docs/dev/api/skimage.feature.html#id55). Cells were counted and recorded automatically to yield the total cell count for the entire section. Then, blob detection of IHC signals (DAB brown color) was done with the criteria that they should overlap or be in very close proximity ($\leq$5um) of the identified nuclear blobs to designate it as positively staining cell. A positive DAB brown color is defined as a color hue intensity of 0.4 and above (we set the DAB threshold $\geq$0.4) in a range of 0–1.0, with 0 being white and 1.0 being the darkest brown intensity found in the image scanned as determined by the algorithm during color deconvolution step. Subsequently, each of the split images and their image enumerated cytometry data were concatenated

and consolidated. Regions for fast image analysis (FRIA) for each layer were identified, and the samples were quantified for percent positive staining per total cells per FRIA. The total number of positive staining cells was divided by the total number of cells to get the percent positive cells measure.

Immunocytochemistry of VICs

VICs from mixed and FACS sorted populations were cultured to semi-confluency in separate 4 cm^2 chambers. Cells were washed three times before fixation with 1.0 mL of 4% paraformaldehyde (PFA) for 10 min. After discarding the PFA and washing with PBS, we added a 2x permeabilization buffer (eBioscience Fix and Perm set Cat# 88-8824-00) mixed in FluoroBrite™ DMEM (Thermo Fisher Cat# A1896701) for 10 min to ensure permeabilization. After washing again, we added 1x permeabilization buffer, 1% PermWash (BD Biosciences, Cat# 554723) in FluoroBrite DMEM solution, and 1:100 primary antibodies to the cells for 30 min at room temperature in the dark while ensuring a gentle shaking. After 2x gentle washing in PBS, the secondary antibody cocktail was prepared with matching specificity to the primary antibody cocktail at 1:500 concentration of the antibody. After 30 min of incubation in the dark, slides were gently washed 3x with PBS. The slides were stained with Hoechst 33543 (BD Biosciences, Cat# 561908), 1:100 in FluoroBrite DMEM for 10 min. After 2x washing with pure FluoroBrite™ DMEM, imaging was done with Nikon Eclipse Ti A1 Confocal microscope in 20x and 60x water immersion magnification.

High throughput screening (HTS) of 242 cellular surface markers in aortic VICs and MSCs

VICs are isolated from calcified aortic valves, while adipose stroma-derived mesenchymal stem cells (MSCs) from a cell-line (ATCC® PCS-500-011™, LOT# 80622175) are cultured in three different conditions. These conditions are undifferentiated (cultured in normal media, NM), osteoblast-like differentiated (cultured in osteogenic media, OM), and adipocyte-like differentiated (cultured in adipogenic, AM media) conditions for two weeks. To release single valvular interstitial cells, we conducted valve tissue digestion, as described above. Clumps, debris, and calcium crystals were removed by thorough washing using a cell strainer (Corning, cat#431752). The cells for each donor valve (n = 8) were counted separately, then pooled in equal proportions per donor. Afterwhich, we analyzed the tissue isolated VICs and the MSCs (cells from each condition per cell type) via high throughput screening flow cytometry (HTS-FC). Each cell suspension per sample condition (i.e., VICs, MSC-NM, MSC-OM, MSC-AM) was adjusted to a concentration of 1×10^6 cells per mL in a 22 mL volume of serum-free DMEM to dispense 250,000 cells per well to the 242 unique single antibody surface marker-per-well kit (BD Bioscience Lyoplate Human Cell Surface Marker Screening Panel, Cat# 560747). MSCs were passaged with Accutase (BD Biosciences) and expanded to 18 150-cm2 flasks, with six flasks per media condition. Cells from culture and cells directly coming from valves were then subjected to a standard FACS protocol (as per kit manufacturer's recommendation) with primary surface marker antibody staining followed by APC-conjugated antibody staining with stringent cell washes in between. They were then fixed with 4% PFA before flow cytometric reading. A BD FACS Canto II with 96-well plate high throughput sampler (HTS) at the Dana-Farber Cancer Institute, Flow Cytometry Core, was used, and data were analyzed using Cytobank and FlowJo version 10.7 software. To compare relative surface marker expression per sample condition, we calculated the percentile rank from percent positive staining measurements. We then took the 85^{th} percentile as the cutoff for categorically labeling that specific CD(n) marker as highly expressed in each sample condition (VICs, MSC-NM, MSC-OM, MSC-AM).

Network analysis of consolidated FACS HTS data with PPI network

There were 16 surface markers that consistently scored >85% percent positive in all three MSC conditions: (1) MSC-NM, (2) MSC-OM, (3) MSC-AM, and VICs, namely: CD13, CD29, CD44, CD47, CD49e, CD55, CD58, CD59, CD63, CD73, CD147, CD151, CD164, beta2-microtubulin, HLA A-B-C, and HLA-B2. To prioritize the 16 surface markers, we took a network approach to determine to what extent these proteins are associated with calcification-related molecules. Beta2-microtubulin, HLA A-B-C, and HLA-B2 are excluded in the analysis as they are known to be expressed in all nucleated cells. The flow cytometry-derived cell expression profiles are rendered in a circular heatmap (Figure 1B). Within this heatmap, the remaining 13 surface proteins were projected onto a curated protein-protein interaction (PPI) network. The 13 markers were used as source nodes (red nodes) to construct a directed interactome network using MetaCore™ (Clarivate). The markers were connected with the shortest paths and a maximum of 2 link nodes (yellow nodes) in the paths. The network was pointed to a calcification-related context by seeding osteocalcin, tissue-nonspecific alkaline phosphatase (ALPL), RUNX2, and osteopontin as markers for calcification end-target nodes (blues nodes). Network topology measurements were done. In particular, the hub and degree centrality were measured using Cytoscape version 3.6 and Gephi version 0.9.1.

3D tissue cell spread immunohistochemistry (IHC)

We used fresh, aortic valve tissues that were not dried excessively or cooled down below room temperature (n = 2). We used Carnoy's fixative method, where we prepared three parts of ethanol in 4°C (or on ice) and 1 part of glacial acetic acid at room temperature. We submerged the valve leaflet (calcified valve) in 45 mL of Carnoy's fixative for 30 min. After fixation for 3-4 h, the fixative was washed off with 70% ethanol using fives changes of fresh ethanol solution. Fixed valves in 70% ethanol could be stored at 4°C for a year without losing the quality of IHC or immunofluorescence (IF) staining quality.

A piece of tissue was pre-warmed to 37°C solution then placed in a Coplin jar containing 1.0 N HCl pre-warmed at 60°C for 8 min to allow for acid tissue digestion. We then rinsed off the tissue using MilliQ water (Millipore) and placed it into a fresh Petri dish containing

45% acetic acid in MilliQ water. After 15 min of incubation, the cells were dispersed into a single cell layer on a microscope slide. In order to disperse the cells, a 0.5 mm × 0.5 mm x 0.5 mm tissue digest was placed on top of a droplet dome of 45% acetic acid solution (~5.0 mL volume) in the middle of a +/+ Superfrost glass slide. On top of the tissue, we placed a 22 mm × 22 mm glass coverslip as a "weight" (Size German #1.5) and gently applied pressure onto the coverslip using fine forceps to spread out the cells. The spreading was monitored using a microscope to ensure that the coverslip was not flattening the cells. Once the cells were spread to a single layer, the glass slide was immediately frozen on dry ice, and the coverslip was gently removed with a razor blade. The glass slide is then ready for immunohistochemistry processing, as described above.

Nuclear morphometry and CellProfiler

We used CellProfiler version 4.0.7 (https://cellprofiler.org/), an automated cell, and nuclear morphometry measuring software package.

Calcification assay of FACS sorted CD44^{+} VICs

Early passage VICs (passage # 1- 4) from cell culture were sorted in Flow Cytometry based on CD44 expression and divided into three groups: CD44^{-}, CD44$^{+,}$ and CD44^{high}. The three groups were then plated into a multi-well plate and grown until confluent. Osteogenic differentiation assays were conducted for three weeks after either OM or NM treatment. We used Alizarin Red (AR) 2% (Fisher Scientific) for osteogenic assays. Cells plated in 48 or 96 well plates were washed with PBS and fixed with 10% formalin for 15 min at room temperature. After washing with Milli-Q water, we added the stain and incubated it for 20 min. After washing 3x with Milli-Q water, we took pictures and quantified the amount of dye released by spectrophotometry at 550 nm.

Mass cytometry (CyTOF)-based protein profiling of aortic VICs

CyTOF uses rare metal isotope-conjugated antibodies to detect and quantify target proteins. A list of CyTOF antibodies is enumerated in the Key resources table. Aortic VICs prepared from collagenase digestion of the tissue recovered overnight in culture (37°C, 5%CO2 incubator) using DMEM with 10% FBS, 1x antibiotic/antimycotic, and 10 mM HEPES. After the overnight culture, the cells composed a non-adherent majority and less than 5% loosely adherent cells. We harvested the cells, washed them with barium-free PBS (Invitrogen), and then pelleted them in a centrifuge at 300g for 10 min. We stained the cells for viability for 5 min at room temperature using Cell-ID^{TM} Cisplatin (Fluidigm) at 5.0 μM concentration in barium-free PBS with cell density at <1 × 10^{7} cells/mL in a 250 μL reaction volume. The viability staining reaction was stopped using a 5x cell suspension volume of MaxPar® cell staining buffer (Fluidigm). All onward steps were carried out using barium-free buffers, reagents, and containers. We again pelleted the cells and resuspended them in 100 μL reaction volume at 1.5–3.0 × 10^{6} cells/mL before fixing 200 μL Fix I buffer (Fluidigm) for 10 min at 4°C. Fixation was stopped by washing the cells with 800 μL cell staining buffer (CSB) (Fluidigm). We permeabilized the cells using a saponin-containing CSB-S buffer (Fluidigm) for 1 min and pelleted them. Next, we incubated the cells with 500 μL nuclear antigen staining buffer (Fluidigm) for 30 min before washing with a nuclear antigen staining perm solution (Fluidigm). The resulting cells were then pelleted at 800g for 5 min and resuspended in 10 μL of the residual volume. Nonspecific antibody binding was stopped using 10μL of 1:100 CSB-S buffer dilution of Human Fc Block (BD Biosciences) for 10 min at room temperature. We incubated the cells for 30 min following the blocking procedure at room temperature (with occasional agitation of the cell suspension) with a 20 μL antibody cocktail. In addition to the antibodies used for FACS as described above, we included eight additional surface antibodies and 14 intracellular marker antibodies. The cocktail was prepared in CSB-S buffer to permeate intracellularly. The antibody binding reaction was stopped by washing the cell suspension with 800 μL of CSB-S and pelleting the cells at 800 g for 5 min. After most of the supernatant was discarded, pelleted cells were again resuspended in 50 μL of the residual volume. Cells were all washed 2x in 800 μL and pelleted at 800g for 5 min. Nuclear content interaction and bead spiking (Fluidigm) were used for every sample. The prepared cells were run in a Fluidigm Helios CyTOF MS machine and analyzed in Cytobank.

Multi-color FACS of aortic VICs

The 13 markers identified in the FACS analysis were tested for co-expression of progenitor and calcification markers by multi-color FACS. To determine surface markers associated with the putative progenitor cell population, each of the 13 markers was tested for co-expression with the other, and co-expression with a marker for calcification (osteocalcin) and a marker for proliferation (Ki-67). The FACS protocol was carried out. We washed and strained cells from valve digestion and then blocked them with a 1:100 concentration of human Fc Block (BD Biosciences, cat# 564219) for 5 min before surface antibody (fluorochrome-conjugated) staining. After staining with surface antibodies, we washed, fixed, and permeabilized the cells with permeabilization buffer containing 1% saponin (eBioscience) to prepare for intracellular marker staining. Staining with a cocktail of osteocalcin and Ki-67 antibodies was followed by stringent cell washes and final cell fixation before FACS reading. FACS data were acquired using BD FACS Aria (BD Biosciences) and analyzed using FACS Diva software.

Fluorescence-activated cell sorting (FACS) of CD44highCD29^{+} CD59^{+} CD73^{+} CD45^{low} population

To isolate the CD44^{high}CD29^{+}CD59^{+}Ki67^{+}OC^{+}D45^{low} disease driver cells (VICs DDP) by flow cytometry, confluent early passage (P1-P4) heterogeneous VICs from at least one 150 cm2 flasks were detached and resuspended in FACS buffer consisting of DMEM, 1% penicillin and streptomycin, 3% FBS and 1 mM HEPES. After centrifugation at 300g for 10 min, cell pellets were

resuspended in an antibody cocktail solution with 4 μL APC-conjugated CD44, 3 μL of AF488-conjugated CD29, APC-conjugated CD59 and PE-conjugated CD73, and 1μL of PE-conjugated CD45 in 200 μL FACS buffer in a microtube. All stock antibody solutions were at 0.5 μg/μL. We kept the sample(s) in the dark and let it incubate while being swirled and mixed at room temperature for 40 min. We added another 1 mL of FACS buffer before a spin-down at 500g for 5 min. After discarding the supernatant, we repeated the washing step with FACS buffer. We resuspended the final pellet in 400 μL of FACS buffer. Two 15 mL receiving tubes were prepared, each with 4 mL of FACS sorting solution containing DMEM, 1% penicillin and streptomycin, 5% FBS, and 10 mM HEPES. Cells matching $CD44^{high}CD29^{+}CD59^{+}CD73^{+}CD45^{low}$ (VICs DDP) were sorted out in one tube and the remaining cells in the other tube using the BD FACS Aria. Sorting efficiency was between 96-99% in purity mode.

Sample preparation for proteomic analysis

Protein isolation and peptide digestion for time course profiling of differentiated MSCs and VICs

In vitro expanded (in normal media, NM) MSCs (passage 3), unsorted valvular cells (VICs MIX), and FACS-sorted valvular cells (VICs DDP) were exposed to a change of culture media into two conditions (done in parallel): (1) normal media, NM (same media) and (2) osteogenic media, OM. In addition, for each condition, the three different cell types were cultured in replicate wells assigned for different harvesting time points after the change in media (NM or OM): day 0, day 7, day 14, and day 21. We also set aside replicate plates for days 14 and 21 of the NM and OM cultures for calcification assessment by Alizarin Red staining (phenotype). We used three technical replicates for the MSC samples, three biological replicates for the proteomic samples, and four biological replicates for the Alizarin red staining (three of which were part of the proteomics experiment while the fourth donor sample intended for proteomic analysis was unfortunately lost during protein preparation steps). At the time of the harvest, the adherent cells were quickly rinsed with cold PBS (3x) then lysed with cold RIPA buffer (Cell Signaling Technology Cat# 9806S) with 1x protease inhibitor cocktail (Sigma, Cat# P8340-5ML). Cell lysates were then stored at −30°C until all harvest time points were reached (day 21). The cell lysates in RIPA buffer (see STAR Methods, *In vitro* modeling of aortic valve calcification) were thawed and slowly passed through a pre-chilled gauge 27 needle using a 1 mL-syringe over ice 20x to facilitate and complete cell lysis. As described above, each of the resulting homogenate-lysates was first processed by sonicating on ice. The protein disk precipitate from the sonicated homogenate was extracted using a 2:1 chloroform: methanol solution through vigorous vortex mixing for 30 s followed by high-speed centrifugation at 18,000g for 30 min at 4°C. Upper and lower liquid phases were discarded, and each protein disk was solubilized in lysis buffer of the iST 96x Kit (iST - 2x LYSE Buffer 10 mL, PreOmics GmbH, Cat# P.O.00027) using 50 μg protein input.

Mass spectrometry

For data-dependent acquisition (DDA, unbiased peptide sampling), we analyzed peptides using the Orbitrap Fusion Lumos Tribrid mass spectrometer (Thermo Fisher Scientific), fronted with an Easy-Spray ion source and coupled to an Easy-nLC1000 HPLC pump (Thermo Scientific). The peptides were separated using a dual column setup: an Acclaim PepMap RSLC C18 trap column, 75 μm × 20 mm; and an EASY-Spray LC heated (45°C) column, 75 μm × 250 mm (Thermo Fisher Scientific). The gradient flow rate was 300 nL/min from 5 to 21% solvent B (acetonitrile/0.1% formic acid) for 120 min, 21 to 30% Solvent B for 10 min, followed by five minutes 95% solvent B. Solvent A is 0.1% formic acid. The instrument was set to 120 K resolution, and the top N precursor ions in 3 s cycle time (within a scan range of 375-1500 m/z) were subjected to collision-induced dissociation (CID, collision energy 30%) for peptide sequencing (or MS/MS).

The MS/MS spectra were queried against the human UniProt database (downloaded on August 01, 2014; with 88,944 sequences) using the HT-SEQUEST search algorithm via the Proteome Discoverer (PD) Package (version 2.2, Thermo Fisher Scientific). The precursor mass tolerance was set to 20 ppm, and the fragment mass tolerance was set to 0.5 Da. Methionine oxidation and n-terminal acetylation were set as variable modifications, and carbamidomethylation of cysteine was set as a fixed modification. Peptides were filtered based on a 1% FDR based on the reverse database (decoy) results. We enabled the ' Feature Mapper ' node to quantify peptide precursors detected in the MS1 but not sequenced from sample to sample.

The chromatographic alignment was done with a maximum retention time (RT) shift of 10 min and a mass tolerance of 10 ppm. Feature linking and mapping settings were RT tolerance minimum of 0 min, a mass tolerance of 10 ppm, and a signal-to-noise minimum of five. Peptides assigned to a given protein group and not present in any other protein group were considered unique. Consequently, each protein group is represented by a single master protein (PD Grouping Feature). Precursor peptide abundances were based on chromatographic intensities, and the total peptide amount was used for normalization. We used unique razor peptides per protein for quantification. Proteins with two or more unique peptides were considered for further analysis. The proteins from each Proteome Discoverer exported dataset were normalized by the protein median intensity. The protein abundance trends (heat maps and principal component analysis) were analyzed using Qlucore Omics Explorer 3.4 (Qlucore AB, Lund, Sweden). Using Qlucore, we also looked for differentially regulated proteins between different sample groups.

Analysis workflow of MSC and VIC time course proteomics

Based on our previous study, we expected that for the VICs, in addition to the time and media condition, a third source of variation would be baseline donor-to-donor variability. Initial PCA analysis of the VIC data showed that samples plotted distances on the PCA plot axes were mainly driven by donor effects, masking the underlying biology related to the differentiation time course. This donor-to-donor variability and effect were removed by factor elimination using a general linearized model in Qlucore OMICs explorer. To

identify similarly expressed proteins in MSCs and VICs as a function of OM-induced differentiation, we performed a series of filtering steps (Figures 5F–5H, S5, and S6). Specifically, for MSCs, we filtered for proteins differentially expressed in OM vs. NM; in parallel, we filtered for those whose abundances increased over time in OM. First, protein abundances were filtered using rank regression across replicates over time (q-value < 0.005). The analysis was conducted separately for the samples in OM and NM. To exclude proteins whose abundance changes are driven by cell culture, we omitted those remaining in the filtering steps for both OM and NM conditions, narrowing the MSC global proteome from 3998 to 328 proteins (q-value < 0.005). In parallel, we performed statistical filtering of differentially expressed proteins (DEP) of the original MSC global proteome by two-group comparison of NM vs. OM at 7, 14, and 21 days respectively (cutoff q-value < 0.005). To prioritize filtering based on media condition and not the confound of time point, we added a factor elimination for a time as described earlier, resulting in a reduction from 3998 to 956 DEP (increase and decrease, inclusive) between OM and NM (Figures 5F and S5).

From the global proteome, sample conditions (MSC-OM, MSC-NM, DDP-OM, DDP-NM, MIX-OM, and MIX-NM) were analyzed separately as two main comparisons initially: (1) MSC-OM vs. MSC-NM, and (2) comparison of DDP-OM, DDP-NM, MIX-OM, and MIX-NM. In the MSC-OM vs. MSC-NM differentially expressed proteins comparison, the analysis was done two ways: a rank-regression across time points (0 weeks, 1 week, 2 weeks, and 3 weeks after either OM or NM culture) and a two-group comparison between media conditions (OM vs. NM). The resulting differentially expressed proteins (DEP) as time progresses from 0 weeks to 3 weeks as filtered through rank regression were consolidated and designated as "DEP MSC-OM." The DEP MSC-OM that increases over time comprise 86 proteins.

In the analysis workflow of DDP and MIX proteomics data (Figures 5H and S6), we performed stepwise filtering of proteins that increase with calcification. To identify differences in the proteome of these VIC samples, each of the conditions was analyzed, as above, in two ways: (1) a rank-regression across time points and (2) a two-group comparison between media conditions. Thus, we performed all filtering steps for DDP and MIX in parallel until the consequent convergence of the data. The first rank regression filtering step resulted in a reduction from 4538 to 1002 proteins (q-value < 0.05) for the VIC-MIX, while the VIC-DDP reduction was from 4444 to 747. The two-group comparison between NM vs. OM conditions filtered 679 DEP for MIX and 629 DEP for DDP VIC (q-value < 0.005). The overlap between the DEP lists from the two statistical filtering schemes for each VIC condition resulted in 330 DEP for MIX and 289 DEP for DDP. For an uncomplicated, straightforward analysis, we further limited the 330 MIX DEP and 289 DDP DEP list by focusing on the set of proteins with an increasing-over-time trend (197 & 169 proteins), analogously to the DEP of MSCs.

Exploring these OM-vs.-NM- and time course-derived DEP lists further may reveal proteins that may explain the phenotypical difference between DDP and MIX. By taking the overlap between the MIX-DEP (197) and the DDP-DEP (169), non-discriminating proteins (shared) can be eliminated from downstream analysis (Figure 5F). There are 97 proteins shared between the MIX (197) and DDP (169), while 71 proteins are exclusive to the DDP (Figures 5I and Table S4, right column). These 71 proteins are differentially expressed over time while being differentially expressed between NM and OM conditions among the DDP.

In vitro modeling of aortic valve calcification

For *in vitro* experiments, either heterogeneous VICs or ones isolated by flow cytometry were expanded in cell culture to conduct proteomics and single-cell transcriptomics in a time course setup. In addition to VICs, human adipose-derived mesenchymal stem cells (ATCC® PCS-500-011™) were used as a positive control in osteogenic media (OM) and as a negative control in growth media (GM). Cells were lysed at time points of 0, 7, 14, and 21 days in OM and GM in either 10% RIPA buffer (CST) in HPLC H_2O containing 1% protease inhibitor cocktail (Sigma) by vigorously scraping the cells with polyethylene cell scrapers to collect them or immediately frozen and stored in −80°C until further processing. The media at the corresponding time points was collected for future Enzyme-linked Immunosorbent Assay (ELISA).

Functional *in vitro* assays (MSCs and VICs)

Osteogenic, chondrogenic, and adipogenic differentiation assays were conducted for samples of protein, RNA, and media collected at 0, 1, 2, and 3 weeks after changing media from growth media to specialized media. Alizarin Red. Alizarin red (AR) 2% (Thermo Fisher Scientific), Alcian blue (AB) 1%, and oil red O (ORO) (Abcam) were used for osteogenic, chondrogenic, and adipogenic assays, respectively. Cells plated in 48 or 96 well plates were washed with PBS and fixed for 15 min at room temperature with 10% formalin for AR and AB and 4% PFA for ORO. After washing with Milli-Q water, stains were added. For ORO, another washing step with propylene glycol (85%) with 2 min incubation was conducted. The incubation times were 20 min (AR), 1 h (AB), and 15 min at room temperature (ORO). Washes with Milli-Q water followed the AR (3x) and AB (4x) stains. For ORO, the wash steps were as follows: propylene glycol for 5 min, followed by 5x washing with Milli-Q water, 2 min incubation with hematoxylin, and a final 5x wash with Milli-Q water was conducted to finish the staining process. Pictures were taken using an iPhone7 (Apple), and the amount of dye released was quantified by spectrophotometry at 550 nm.

Computational analysis of proteomic data and network analysis

Using the multi-group comparisons with FDR <0.5, we statistically filtered the proteomic data between the different groups. Using Qlucore, we conducted a network-based analysis, including pathways enrichment to find significant disease associations and potential therapeutic targets among 'hub' nodes using the proprietary computational algorithms of MetaCore™ (Clarivate Analytics/Thompson Reuters). In addition, we built subnetworks of the filtered proteomics data and calcification and DDP surface

markers using a global map of human protein-protein interactions (PPI). The human PPI network consists of curated physical PPIs with experimental support, including binary interactions, protein complexes, enzyme-coupled reactions, signaling interactions, kinase-substrate pairs, regulatory interactions, and manually curated interactions from literature, the details of which were described previously. The subnetworks depicted in Figure 6H were constructed by mapping the filtered proteomics data and calcification and DDP surface markers, along with their direct interactors (first neighbors), onto the PPI network using the Networx library v1.9 in Python v2.7.10. Shared proteins between subnetworks were identified to determine the overlap between subnetworks. The statistical significance of the overlap between subnetworks was calculated using a two-tailed Fisher's exact test. Networks were visualized using Gephi v 0.9.2.

Single-cell transcriptomics

All single-cell experiments were conducted in the single-cell core facility of the Harvard Medical School.

Single-cell isolation via InDrops and cDNA library preparation

Cells were detached from culture by adding 1.0 mL/10-cm2 area of Accutase (BD Biosciences) and incubating at room temperature for 3 min. VICs normal media (5% FBS + DMEM) was added to stop the enzymatic digestion. Single-cell dispersion and preparation were achieved by gently pipetting up and down 20x and passing the cells through a 70 um cell strainer (Corning). Cells were then immediately sorted and processed using in-droplet barcoding, according to a previous report.

cDNA library preparation and sequencing

The cDNA library was prepared using the CEL-Seq/MARS protocol (Ziegenhain et al., 2017) with quality control analysis done with Agilent Bioanalyzer. Superscript III Reverse Transcriptase (Invitrogen)/cell lysis mix was encapsulated *a priori* in the hydrogel droplets together with primer beads. We sequenced with an Illumina NextSeq sequencer using a multi-read approach. The first read acquired the barcodes of the samples and the universal molecular identifiers (UMI) sequences, while the second read mapped the results to a reference transcriptome. Sequencing was done at the Dana-Farber Cancer Institute Molecular Biology Core Facilities (MBCF).

Single-cell analysis

Raw data processing to normalized UMI-filtered counts

Post sequencing, raw FASTQ data files underwent bioinformatics processing via bcbio/bcbio nextgen-seq, a python toolkit (https://github.com/bcbio/bcbio-nextgen) and algorithm pipeline. Briefly, Nextseq reads were assigned to each cell by matching the cellular barcodes followed by the UMI extraction for each read, https://doi.org/10.1101/073692. The reads were then aligned to the hg38 transcriptome (augmented with the transgene) using RapMap (http://doi.org/10.1093/bioinformatics/btw277), and counts of reads per transcript per unique UMI were generated for each cell. A multi-step quality control aimed to filter out any noise in the raw data was performed. As a first step, only cells with more than 1,000 reads were kept using the bcbio filtering pipeline. The distributions of reads per cell, UMIs per cell, genes per cell, and mitochondrial ratio per cell were used to define cutoffs further, thus identifying cells with high-quality RNA. Additional QC metrics applied include UMIs vs. genes detected, UMIs vs. read counts, and a novelty score. The novelty score method helps filter out cells with fewer genes detected per count than other cells by looking at the genes per UMI. The final data was exported in a cell by gene matrix for each sample. Data preparation was conducted at the Harvard T. Chan Bioinformatics core facility.

SeqGeq analysis

QC-processed data was analyzed using SeqGeq software with plugins (http://exchange.flowjo.com). As a first step, each necessary sample-condition cell population for the analysis was concatenated as one file. A cell dispersion plot was used from this concatenated file to exclude any doublets missing from the bcbio QC doublet exclusion algorithm. We found almost no doublets in our post-bcbio analysis. A gene dispersion plot was used to gate out highly expressed and very lowly expressed genes ($\leq$10 genes per cell) globally. Filtering out these ''outlier'' genes was necessary since very high expression among all cells may be indicative of housekeeping features or mitochondrial genes, while very lowly expressed genes (expressed in $\leq$10 cells) may contribute noise to downstream clustering and are most likely low quality reads. Gene data points falling within the 10-1,500 × 10-1,500 gate window were labeled ''outlier-filtered genes, OFG,'' which are free of the outlier genes (highly expressed $\geq$1,500 counts/cell or lowly expressed $\leq$10 counts/cell). By switching to gene view, using only the OFG set, we plotted genes in a scatterplot bound by axes of ''cells expressing-'' vs. ''gene dispersion'' features and gated for the highly dispersed genes (HDGs) that vary expression considerably among cells. This gate excluded plot coordinates coinciding with the ''control'' spiked RNA species. These external RNA controls Consortium (ERCC) RNA InDrops spiked sequences served as non-varying control RNA species within our samples and confirmed the appropriate boundaries of the HDGs gating strategy and testing for batch variability among samples. The HDGs gene set was used as the basis for computing for the single cells' principal component analysis (PCA) visualization.

High dimensionality reduction was initially accomplished by PCA using the highly dispersed/varying gene expression of the HDG gene set. The resulting top 25 PCA components describe the gene parameters that explain the majority of the gene expression variance among cells. These may be due to the sample condition, the cell type of the samples, or intrinsic cell population heterogeneity within each sample-condition. Subsequently, the top 15 PCA components were used to conduct non-linear dimensional reduction through t-Distributed Stochastic Neighbor Embedding (t-SNE). The resulting t-SNE plots clustered cells based on global gene variance. In conjunction with multigraph color mapping, the phenotype of ''islands'' of cells in t-SNE space becomes apparent. Using stepwise filtering of highly variant genes from QC to PCA to t-SNE mapping was particularly effective in clarifying cell cluster ''calling.''

Differentially expressed gene (DEG) analysis of single-cell transcriptomics

After initially analyzing all six samples (MSC-OM, MSC-NM, PUR-OM, PUR-NM, MIX-OM, and MIX-NM) as one concatenated data frame, we found that MSC samples tend to cluster distinctly from the VIC samples, suggesting that few gene expression patterns are shared between VICs and MSCs, despite the polarizing effect of either the osteogenic media (OM) or normal media (NM), Figure S4A. To derive potentially shared biology between the OM-modeled VICs and the prototypical vascular calcification model (OM) MSCs, we analyzed MSCs and VICs as separate (but with concatenated same cell type) files. The resulting two differentially expressed gene sets (MSC- and VICs-specific) were then analyzed as two separate omics summaries. Therefore, we analyzed the MSC dataset first separately. We processed the MSC dataset using SeqGeq as above. This time we used HDGs only from the MSC dataset. The resulting PCA processing revealed that only the top 6 principal components (PC) were needed to create a tSNE plot because the top 6 PC explains most of the variability of the MSC dataset. Then, k-means clustering was done using these top 6 PC components to separate the cells into six k-means clusters. We decided to limit ourselves to 6 clusters because it only takes the 6 PCA components to explain most MSC variability. Intuitively, we interpreted this to mean that the MSC dataset may be minimally separated into 6 "communities" if it takes 6 PCA components to explain most of the variability. To recreate distinct clusters on the tSNE plot, we simply performed a redundant tSNE plotting this time using the 6 PCA components plus the k-means components (class/cluster assignments based on k-means clustering), resulting in a secondary final tSNE plot (Figures 4A and 4B).

We processed the VICs dataset similarly and found that only 6 top PCA components can explain most of the variability in the VICs dataset. Because of this, we processed the data in the same fashion as the MSCs to get a final tSNE plot showing a good separation of VICs k-means clusters (Figures 4D and 4E). We first filtered for increased differentially expressed genes (DEGs) among the MSC-OM samples by volcano plots of fold change vs. -log (10) q-value (false discovery rate, FDR). There are 43 DEGs in the MSC-OM with an increased fold change of $\geq$1.5 at q-value $\leq$ 0.05 relative to the MSC-NM (Figure 4F, blue and red sample heatmap annotation). Upon comparing each MSC-OM cluster, however, we found no set of DEGs that would uniquely mark one MSC-OM k-means cluster over another, suggesting that MSCs being a cell line is much less heterogeneous than we initially expected. However, the seeming heterogeneity plotted after tSNE, and k-cluster differentiation is explained by the fact that the clustering of MSC-OM cells depended mainly on the similarity of transcript counts (intensity of expression) for each of these 43 OM-DEGs within MSC-OM cells belonging to the same k-means clusters. Still, by interrogating the expression of a known osteoblast-associated marker, SPARC (Figures 4F and S4B), we identify the MSC k4 cluster as the most "pro-calcifying" cluster of MSC cells. By filtering only the DEGs in k4 MSC over k2 (MSC-NM) at FC $\geq$ 1.5 q $\leq$ 0.05 (Figure 4B), we identify 49 DEGs (Table S2) that may be applicable as calcification targets for VICs as well.

We analyzed the VICs dataset similarly and identified that the k4 k-means cluster is the most interesting cluster to explore (see Results). Therefore, we compared the k4 cluster against the combined k1 and k2 clusters, which contain mostly VIC-NM cells (DDP and MIX) to identify enriched DEGs by plotting volcano plots and gating for genes that have a fold change $\geq$1.5 and -value $\leq$ 0.05.

In vitro silencing

Silencing experiments were performed in VICs cells from human AOVs (n = 3). Cells were plated in 48 well plates and were treated with siControl, siMAOA, and siCTHRC1 siRNAs. Lipofectamine RNAiMAX Transfection Reagent (Thermo Fisher) was used per the manufacturer's protocol for this experiment. Before transfection, cells were treated with normal medial and osteogenic media. Silencing experiments were performed using each siRNA in each media condition. Cells were harvested at two different time points for RNA extraction (3 and 10 days). For TNAP activity, cells were harvested in 10 days. Transfection was repeated every 3 days.

RNA purification and cDNA synthesis

RNA isolation was accomplished using the Illustra^{TM} RNAspin mini kit (GE Healthcare, Cat# 25-0500-72). RNA Lyse solution from the Illustra RNAspin Mini Kit (GE Life Science) mixed with 1% 2-mercaptoethanol (Sigma) was added to the adherent cells. Each lysate was frozen at -30°C until further purification. RNA purification was done per the manufacturer's protocol with the GE Healthcare Illustra^{TM} RNAspin Mini Isolation Kit (lot 1711/001). The final purified RNA was eluted in 16 μL RNase-free H2O for a high RNA concentration. The concentration of each sample was measured using a NanoDrop Microvolume Spectrophotometer 2009 (ThermoFisher). To normalize the amount of RNA used between samples, we calculated the volume needed for each sample to have 500 ng of RNA. Complementary DNA (cDNA) was made using the qScript cDNA Synthesis Kit (Quantabio). The volume of RNA was added to a strip tube and diluted with nuclease-free water to a total volume of 15 μL. We added 4 μL of reaction mix and 1 μL of reverse transcriptase (RT) per strip tube. After centrifugation, the prepared strip tube plate was processed for cDNA synthesis in Biosystems 2720 Thermal Cycler. The final samples were stored at 4°C.

Pre-amplification

Pre-amplification of cDNA samples was performed using the Perfecta PreAmp SuperMix (5X) kit (VWR, Cat# 89409-170). An assay primers pool using 2 μL of each primer and additional $T_{10}E_{0,1}$ buffer (10mM Tris-HCl (pH 8.0), 0.1mL EDTA) to reach 200μL total volume was made. The pre-amplification reaction mixture for TaqMan assays with a total volume of 20ul was mixed, using 4μL of PerfeCTa PreAmpl SuperMix (5X), 2.5 μL of TaqMan Assay Pool, 5 μL of cDNA, and 8.5 μL of nuclease-free water. Each sample was incubated in a thermal cycle, following these steps: Initial denaturation (95°C, 2 min), PreAmpl cycling (14 cycles of 95°C, 10 s; 60°C, 3 min) and hold (4°C). Concurrent samples were then used for qPCR.

Quantitative polymerase chain reaction (qPCR)

For qPCR analysis, we used a 384-well plate with 2μL of PreAmp cDNA and 8μL of primer cocktail per well. The primer cocktail was made with 5μL of TaqMan Fast Universal PCR Master Mix (2X), 2.75μL of nuclease-free water (QuantaBio), and 0.25μL of respective primer. PCR was performed using 79020HT Fast Real-Time PCR Systems. Data analysis was made using Prism GraphPad 8.

Tissue nonspecific alkaline phosphatase activity (TNAP) assay

TNAP assay was done using the Alkaline Phosphatase Activity Colorimetric Assay Kit (BioVision, Inc, Cat# K412-500) as per the manufacturer's recommended protocol. Each of the sample lysates was taken from a well of a 48-well plate in triplicates. Measurements were calibrated against a standard curve and normalized with protein amount.

Functional *in vitro* assays to assess MAOA and CTHRC1

VIC cells isolated from CAVD valves were cultured to the third passage before functional assay to validate identified potential calcification targets MAOA and CTHRC. Upon reaching confluency, cells were treated with non-specific siRNA and MAOA or CTHRC siRNA for ten days. On day 10, intracellular alkaline phosphatase assay (BioVision, CA) and qPCR (MAOA, CTHRC, Osteocalcin, and Vimentin) were performed on replicate sample-condition wells. To further prove the functional effect of MAOA inhibition, small molecule inhibitors moclobemide (10 μm) and pirindole (3 μm) were used in separate experiments instead of siRNA. Alizarin red staining was used to evaluate calcification at day 21 post small molecule treatment.

QUANTIFICATION AND STATISTICAL ANALYSIS

Flow cytometry data were quantified using the software FlowJo version 10.6 (FlowJo) and Office Excel 365 (Microsoft) and visualized using R version 4.0 (www.cran.r-project.org). The network of nodes were created using MetaCore (Clarivate) using shortest paths analysis limited to only 2 paths. The resulting network was reconstructed and analyzed for hub centrality by measuring network topology using Cytoscape version 3.6 and Gephi version 0.9.1. The statistical test for comparing two groups in assays (qPCRs, TNAP ELISA, histologic morphometry, etc.) used is an unpaired t-test, non-parametric, Mann-Whitney test, 2-tailed p-value on biological replicates with 2-4 technical replicates for each sample, using the statistical software Prism version 8 or version 9.3.1 (GraphPad). Nuclear morphologies were measured using CellProfiler version 4.0.7, and a comparison between three groups of cells was made using a Wilcoxon non-parametric rank-sum statistics via R version 4.0 (https://cran.r-project.org). CyTOF data was preprocessed using CyTOF Helios software version 6.0 (Fluidigm) and then analyzed (SPADE trees) using Cytobank software version 7.0 (Cytobank-Beckman Coulter) and FlowJo v10.6. For scRNAseq, differential gene expression between two groups was statistically filtered using a false discovery rate (q-value) of <0.05, using the software SeqGeq version 1.6 (FlowJo/BD Biosciences). As mentioned above, scRNAseq data (cell-by-gene matrix and abundances) were processed from raw FASTQ files using bcbio/bcbio nextgen-seq, a python toolkit and algorithm pipeline (https://github.com/bcbio/bcbio-nextgen). The scRNAseq data visualization was done using Plotly dashboard (www.plotly.com), SeqGeq, and MS Office Excel. For proteomics, differentially expressed proteins were calculated between two groups (two-group comparison) as a ratio of averaged median-normalized abundances with statistical filtering using a false discovery rate (q-value) of <0.05, using the software Qlucore Omics Explorer version 3.4 (Qlucore), after getting processed data (proteins list and abundances) from RAW files (mass spectra data) using Proteome Discoverer (Version 2.2, Thermo Fisher). Rank regression analysis (FDR <0.05) in proteomics data was also done using Qlucore v3.4. Statistical details can be found in this section and in the figure legends.

Cell Reports, Volume *39*

Supplemental information

A disease-driver population within interstitial cells of human calcific aortic valves identified via single-cell and proteomic profiling

Julius L. Decano, Yukio Iwamoto, Shinji Goto, Janey Y. Lee, Joan T. Matamalas, Arda Halu, Mark Blaser, Lang Ho Lee, Brett Pieper, Sarvesh Chelvanambi, Jessica Silva-Nicolau, Francesca Bartoli-Leonard, Hideyuki Higashi, Haruki Shibata, Payal Vyas, Jianguo Wang, Elena Gostjeva, Simon C. Body, Sasha A. Singh, Masanori Aikawa, and Elena Aikawa

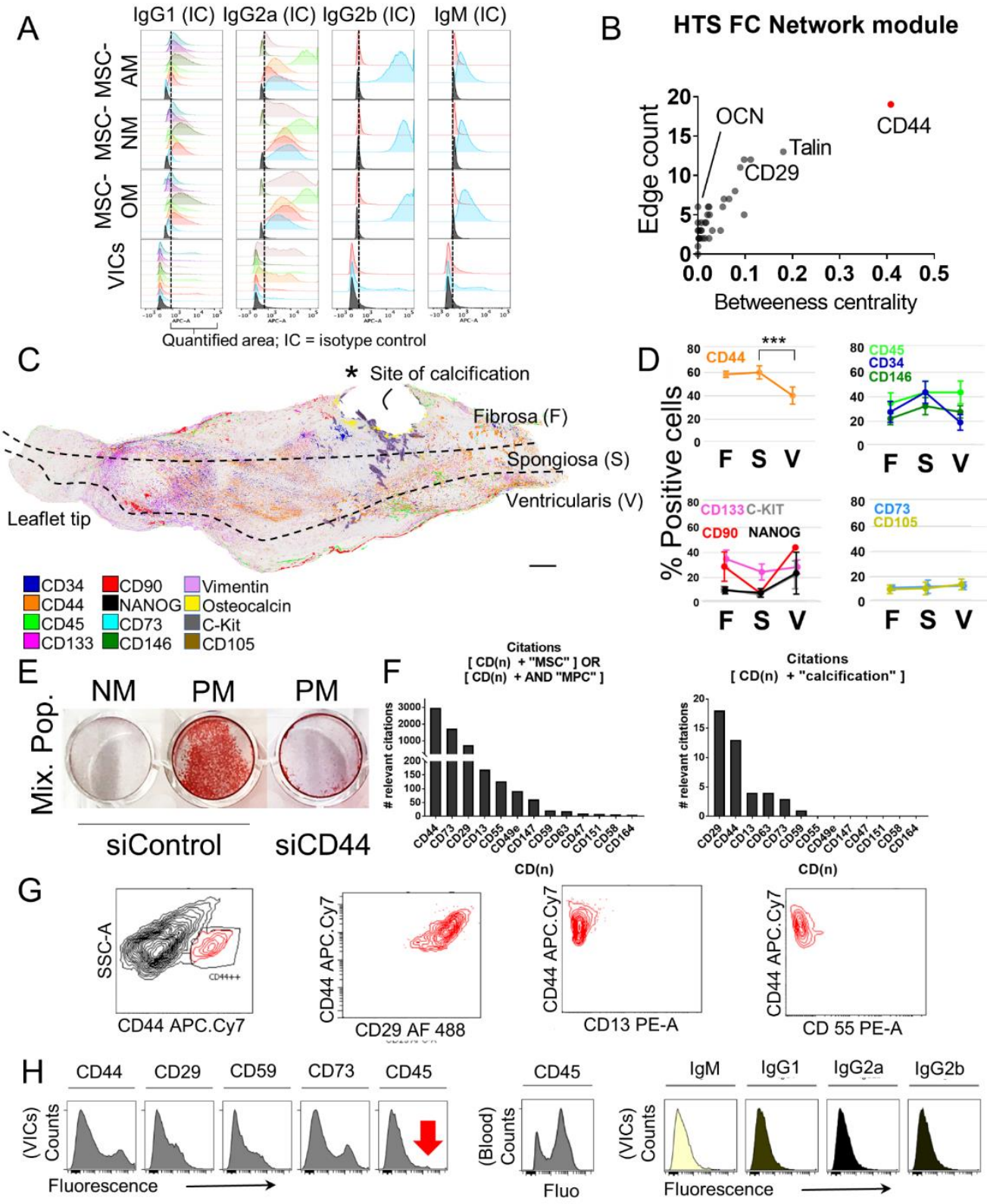

Figure S1. **Combined FACS-derived data, network prioritization, multiparametric immunohistochemistry, literature mining, and in vitro loss-of-function experiment identify CD44 as a central marker in VIC calcification.** Related to Figures 1 and 3. **A.** Histogram of FACS staining in each condition: MSC-AM, MSC-NM, MSC-OM, and freshly isolated VICs from CAVD donors. Threshold limits (vertical dashed gray lines) are determined using isotype controls (IC). Each marker antibody staining profile is matched with their corresponding IC. Histograms of the relative abundance scale

of positive staining frequency of selected surface markers having high expression in all cell conditions. Two conditions (VICs and MSC-OM) with their respective isotype controls (IC) (presented as dark grey). **B.** Plotting edge counts vs. betweenness centrality shows CD44 as the most overly connected node in this "calcification" network, having both the highest edge count and betweenness centrality measure. **C.** Representative IHC staining of a calcified aortic valve leaflet. Positive marker IHC stains are pseudo-colored to facilitate visualization and quantification of markers. **D.** Percent positive stained cells per layer quantified based on the average on ten donor valves. (***) $p < 0.001$. **E.** Silencing CD44 in an unsorted mixed population of VICs resulted in reduced calcification even under culture conditions of pro-calcifying media (PM) via Alizarin red staining. **F.** PubMed literature search of relevant citations associating each of the HTS-FC-identified most abundant markers with the terms: "mesenchymal stem cells" or "mesenchymal progenitor cells" were ranked for frequency. Search for relevant citations associating each of these same markers with the term "calcification." Only six markers satisfy the criteria of having both relevant citations associated with the terms MSC/MPC and calcification: CD13, CD29, CD44, CD59, CD55, and CD73. **G.** $CD44^{High}$ cells co-stain with CD29 but not CD13 or CD55. IHC= immunohistochemistry; PPI= protein-protein interaction; MSC = mesenchymal stem cells; VICs = valvular interstitial cells. **H.** Single color-surface marker antibody staining of VICs and isotype controls. CD45 staining comparison with blood cells as staining reference. VICs have very low staining of CD45 compared to CD45+ human blood cells.

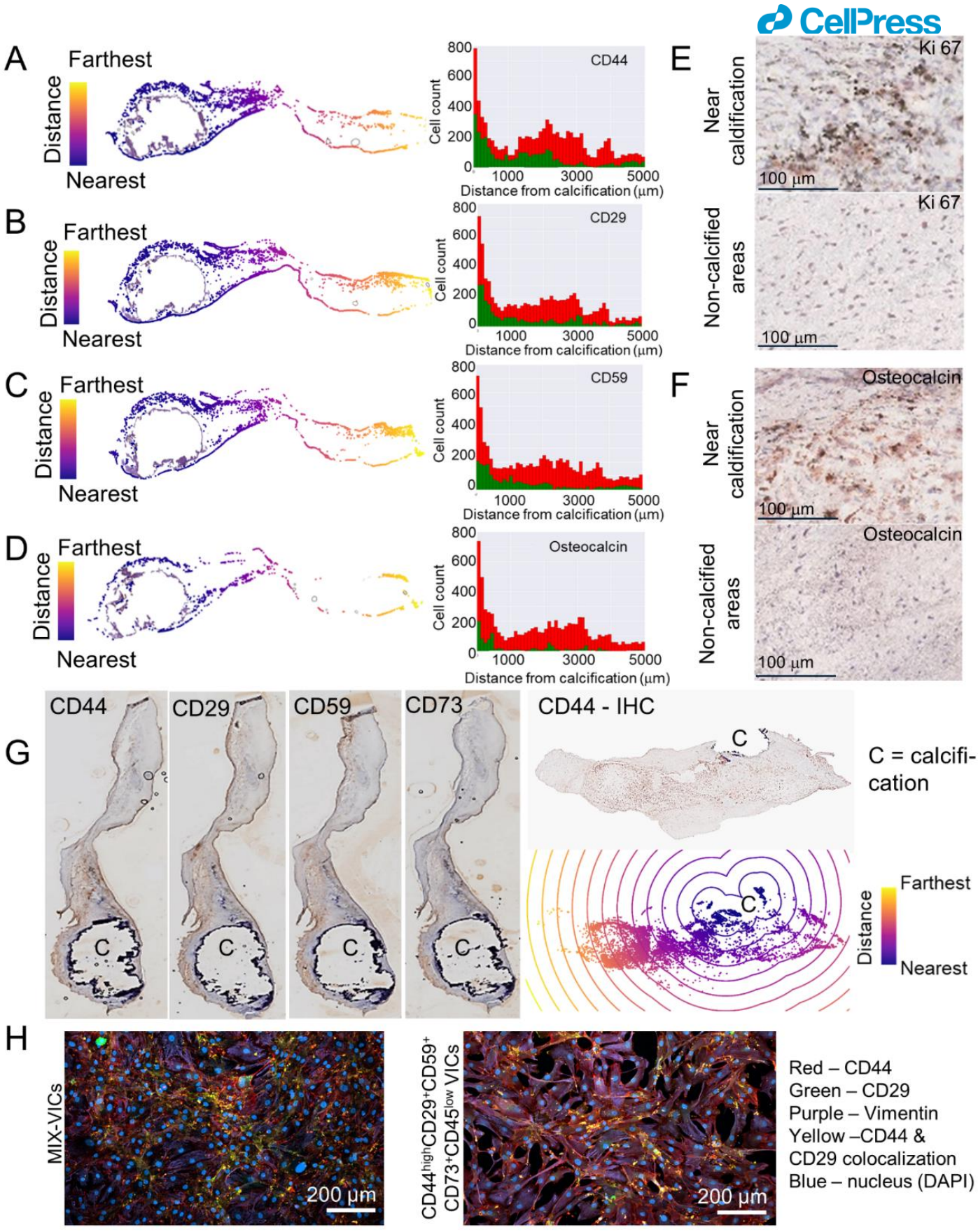

Figure S2. CD44 and CD29-positive VICs contain putative progenitor niches and localize near calcification areas. Related to Figures 2 and 3. **A.** Quantitative distance mapping of positively immunostained cells from the edges of calcification in calcific aortic valve sections. Quantitation of IHC staining of (**A.**) CD44,

(**B.**) CD29, (**C.**) CD59, and (**D.**) Osteocalcin. Colored dots represent positively stained cells (pseudo-colored for counting). Bar plots represent the frequency of positively staining cells (green bars) and total cells (red bars) identified through nuclear staining (H&E). The X-axis represents the distance from the edge of calcification. Y-axis represents the cell count. **E.** Enzymatic IHC of VICs in areas proximal to the calcified area or distal (non-calcified) area with proliferation marker Ki-67, and **F.** calcification marker, osteocalcin **G.** Whole valve imaging of surface marker staining of CD44, CD29, CD59, and CD73, representative image. Distance mapping and quantification of marker staining relative to distance with calcification. **H.** Fluorescent ICC of cultured VICs either as an unsorted mixed population of VICs (MIX) or sorted $CD44^{high}CD29^{+}CD59^{+}CD73^{+}CD45^{low}$ VICs. Markers were detected using AF594 Anti-CD44, AF488 Anti-CD29 (green), and AF647 Anti-Vimentin antibodies (red). Colocalization of signals appears as yellow. DAP – nuclear stain (blue). Vimentin (pseudocolored purple/magenta).

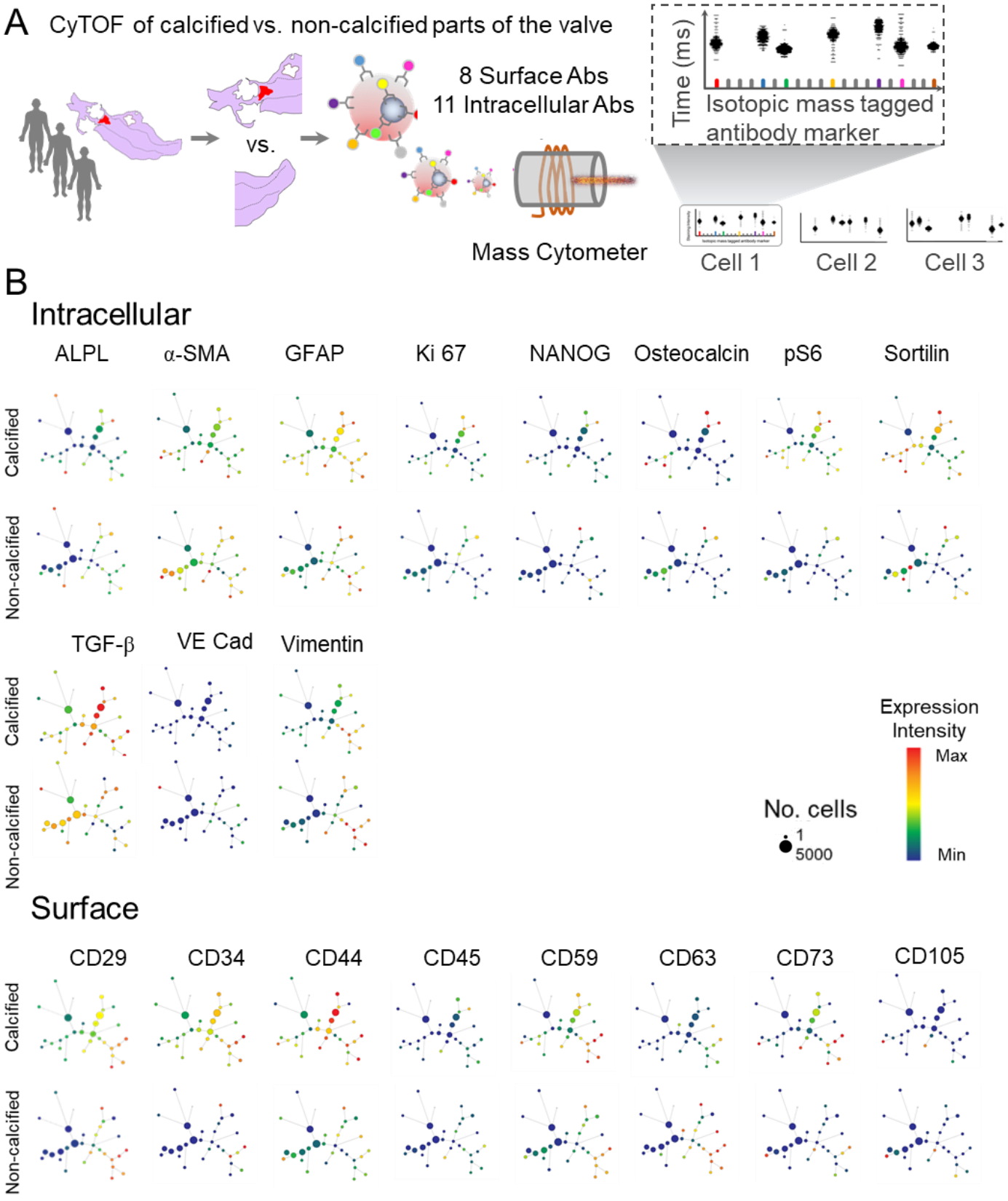

Figure S3. CyTOF profiling of VICs from calcified part of the valve and non-calcified part. Related to to Figure 3H and 3I. **A.** CyTOF or mass cytometry allows for high parametric staining of protein markers in the cells by using rare earth metal tagged antibodies and their unique mass spectrometry detection **B.** 11 intracellular antibodies were used, demonstrating more cell staining in ALPL, GFAP, Ki-67, Osteocalcin, sortilin,

and TGF-beta in VICs from the calcified portion of the valve than in the non-calcified portion. For surface marker staining, calcified area SPADEs contained more cells with higher expression intensities of CD29, CD44, CD59, and CD73 compared to non-calcified area SPADEs.

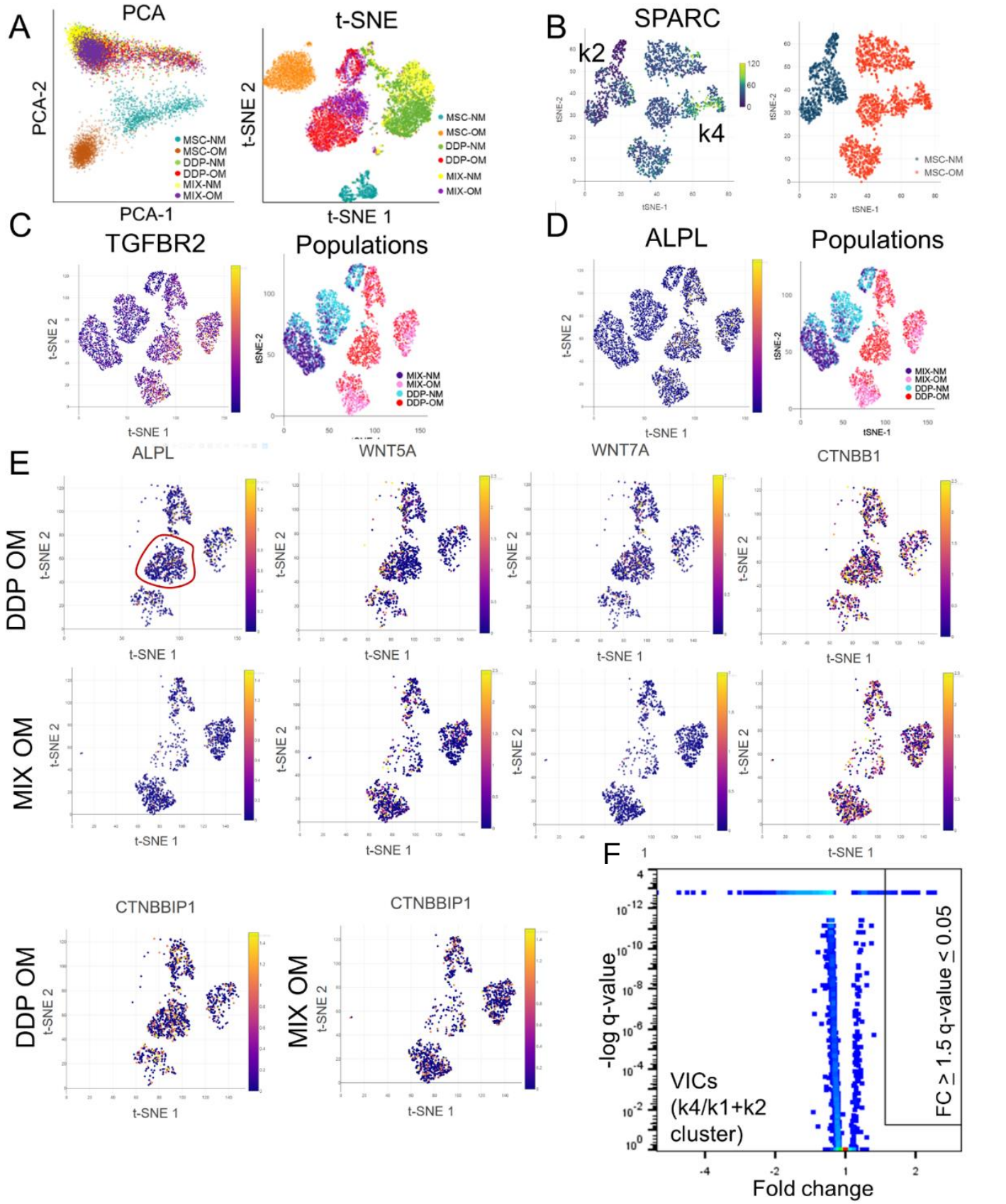

Figure S4. Single-cell transcriptomics of MSCs and VICs, NM vs. OM conditions. Related to Figure 4. **A.** Principal component analysis (PCA) of combined (concatenated) MSC and VIC (DDP and MIX) conditions, NM and OM (left panel),

and corresponding t-SNE projection after using top 6 principal components that accounts for most of the variance among cells to make further dimensionality reduction, tSNE (right panel). **B.** Osteoblast-associated differentiation marker, SPARC expression between MSCs (MSC-NM and MSC-OM) indicating high expression in cluster k4 as seen in the heatmap. k2 is composed of MSC-NM cells, k4 is composed of MSC-OM cells **C.** Osteoblast differentiation marker TGFBR2, and ALPL (**D.**) is also increased in a cluster of VICs where the DDP-OM and MIX-OM are found (red and pink dots) **E**. ALPL, WNT5A, and WNT7A comparative expression is higher in more cells among DDP-OM. Cells than in MIX-OM and are especially concentrated on the k4 cluster**.** Beta-catenin CTNNB1 and beta-catenin interacting protein 1, CTNNBIP1 expression similarly is increased in DDP-OM cells over MIX-OM cells with more expressing cells in the k4 cluster. The gated population of cells in red is the k4 cluster, which is mostly composed of DDP-OM cells **F.** Volcano plot of VICs k4 cluster (DDP-OM) over k1 and k2 cluster (NM). Rectangular gate identifies 34 genes with fold change (FC) $\geq$ 1.5 at q-value (FDR) $\leq$ 0.05. MSC- adipocyte-derived mesenchymal stem cells (ATCC), VICs=aortic valvular interstitial cells, NM=normal media (5% fetal calf serum in DMEM), OM=osteogenic media. DDP=disease driving population (sorted VICs), MIX=mixed VICs population (unsorted)

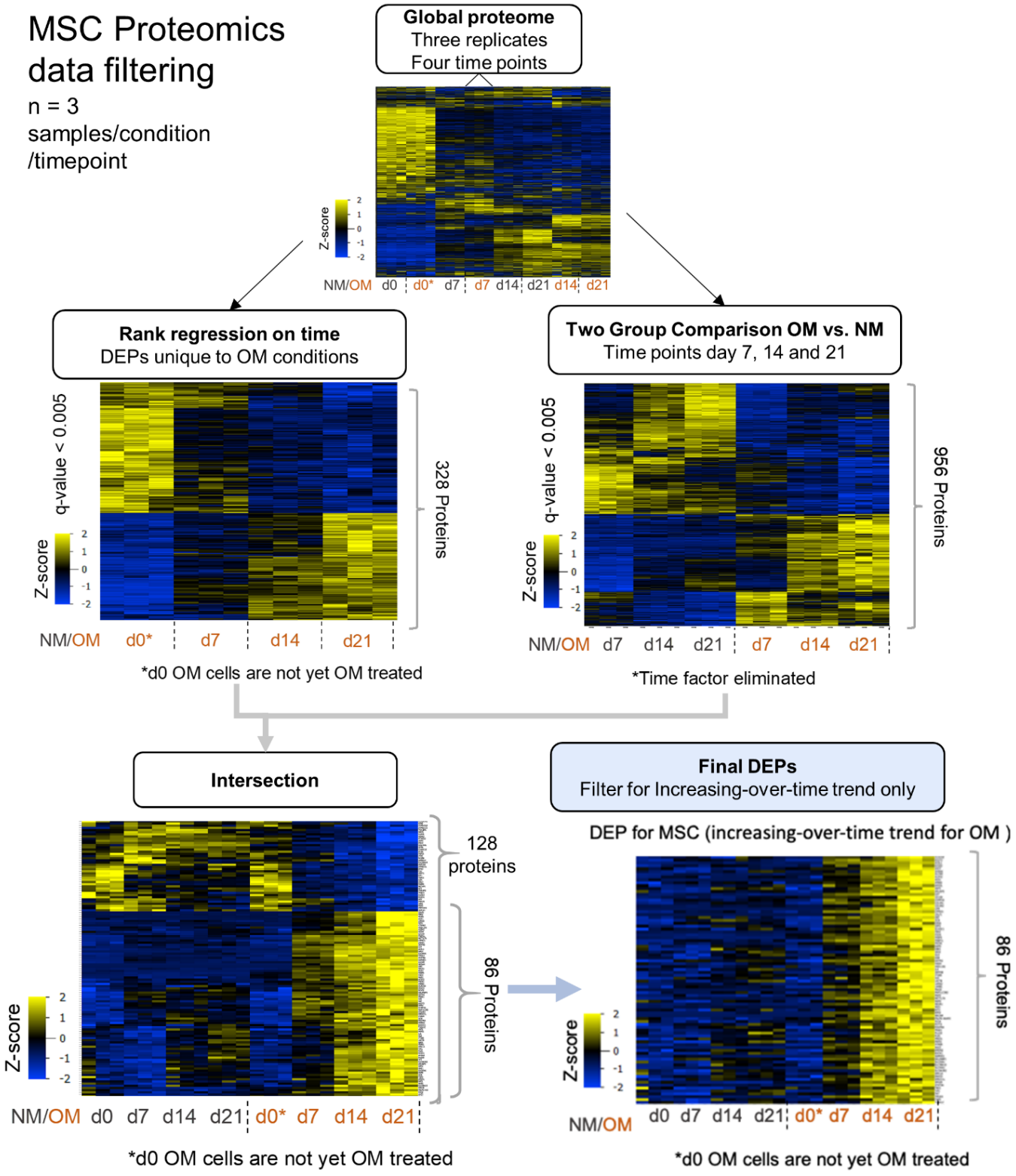

Figure S5.Workflow analysis of MSC proteomics. Related to Figure 5. The heatmap shows proteins as variables in rows while sample conditions are columns. Each sample condition contains biological triplicates (n=3 donors, 1 donor/column). The global proteome is analyzed two ways: (1) rank regression comparison for the increasing time points (r >1), and (2) two-group comparison between the two media conditions (NM and OM, $r \neq 0$) with time factor effects eliminated. We took the intersection between these two analyses to produce a differentially expressed protein (DEP) profile, and then filtered only for the increasing proteins in time and with OM stimulation to arrive at a list of 86 proteins designated as the Final DEPs or the DEPs for MSCs (see Fig. 5G). OM= osteogenic media, NM=normal media, d(n)=day (n) after media stimulation. Analysis was done using the software Qlucore Omics Explorer version 3.4 (Qlucore, Inc.)

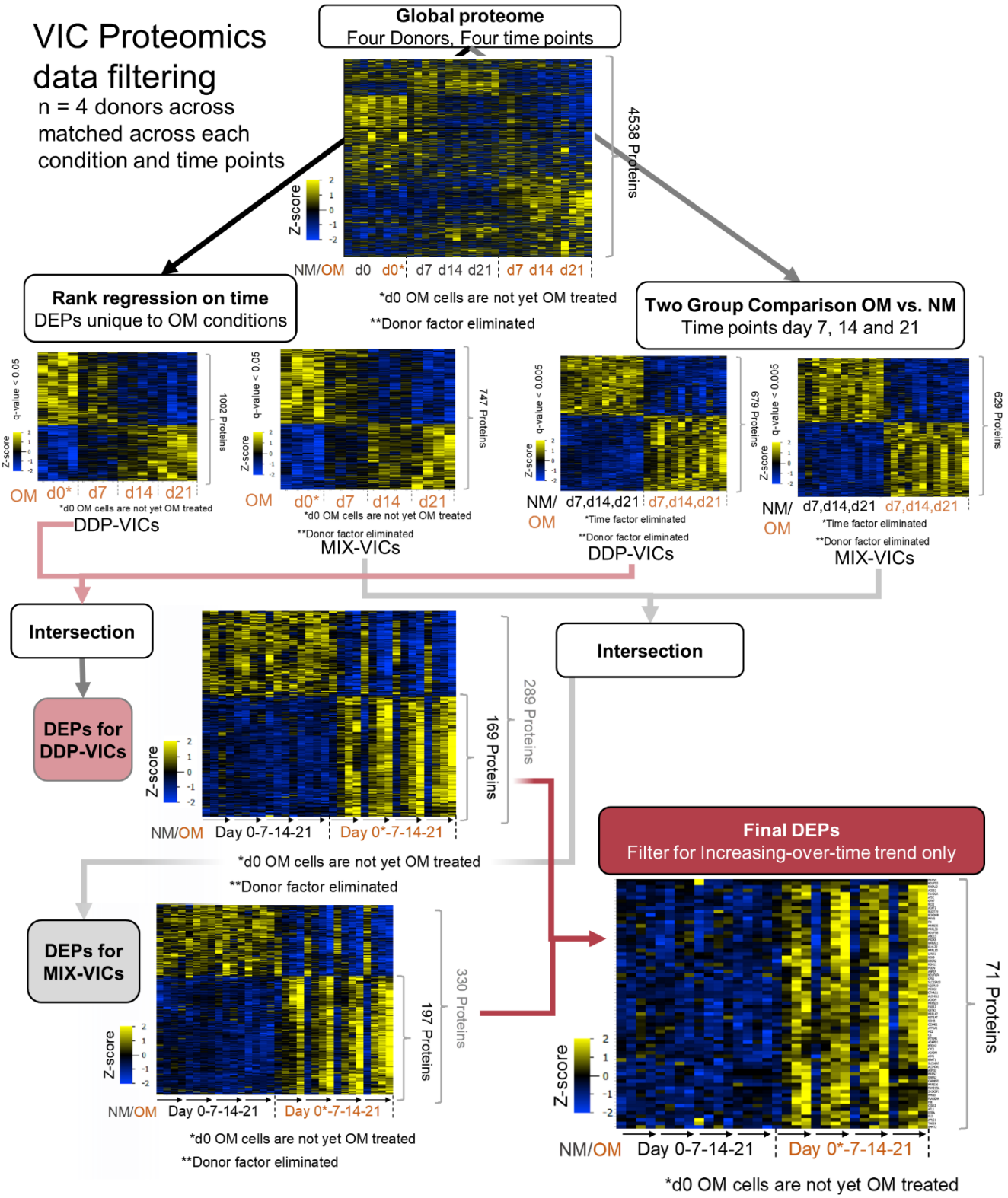

Figure S6.Workflow analysis of VICs proteomics. Related to Figure 5. The heatmap shows proteins as variables in rows while sample conditions are columns. Each sample condition contains biological triplicates (n=3 donors, 1 donor/column).). The global proteome is analyzed two ways: (1) rank regression comparison for the increasing time points (r >1), and (2) two-group comparison between the two media conditions (NM and OM, $r \neq 0$) for either DDPs or MIX. We took the intersection between these two analyses (rank regression and two-group comparison) to produce a differentially expressed protein (DEP) profile, and then filtered only for the increasing proteins in time and with OM stimulation to arrive at a list of 169 proteins for the DDP-VICs and 197 proteins for the MIX-VICs. We then filtered for increasing DEP proteins exclusive to the DDP-VICs arriving at 71 proteins designated as the Final DEPs or the DEPs for DDP-VICs (see Fig. 5I). OM= osteogenic media, NM=normal media, d(n)=day (n) after media stimulation.

Table S3: Differentially expressed genes (DEG) comparing VIC-OM versus VIC-NM and each VIC-OM k cluster over VIC-NM. Related to Figure 4. DEGs are genes **increased** by a fold change of ≥ 1.5 at q-value ≤ 0.05. Each VIC-OM cluster (either DDP-OM or MIX-OM): k3, k4, k5, and k6 is compared against VIC k-means clusters that contain only VIC-NM cells (either DDP-NM or MIX-NM).

DEG of VIC-OM k clusters over VIC-NM only k clusters.	Differentially expressed genes (DEG) for each VIC-OM k cluster (k3, k4, k5, and k6) over the VIC-NM cluster						
	k3 cluster	*k4 cluster*	*k5 cluster*				*k6 cluster*
ANPEP	ACTA2	ANKRD1	ANLN	BUB1B	DLGAP5	KIF20B	ANPEP
CFH	CFH	ANPEP	ANP32E	BUB3	DNAJC9	KIF23	CFH
COL8A1	COL3A1	CCDC68	ARL6IP1	CCNA2	DNMT1	KIF2C	COLEC12
CTHRC1	COL4A1	CD34	ASF1B	CCNB1	DTYMK	KIF4A	CTHRC1
ELN	COL8A1	CFH	ASPM	CCNB2	E2F1	KPNA2	EGR1
FKBP5	CTHRC1	COL8A1	ATAD2	CTHRC1	ECT2	MAD2L1	FBLN1
HIF1A	EGR1	CTHRC1	AURKB	DEK	ELN	MCM2	FBXO32
IGF2	ELN	ELN	BIRC5	DEPDC1	FAM149B1	MCM3	FKBP5
KCNT2	FBLIM1	HIPK2	BUB1B	DHFR	FAM83D	MCM6	FOS
METTL7A	FBLN1	IGF2	BUB3	DLGAP5	KIF20B	MKI67	GAS1
NID2	FBXO32	IRS2	CCNA2	DNAJC9	KIF23	MT2A	HIF1A
PHACTR2	HIF1A	ITGA5	CCNB1	DNMT1	KIF2C	MTHFD1	ID1
PROS1	IGF2	KCNT2	CCNB2	DTYMK	KIF4A	NCAPD2	IFITM2
PTGS1	IRS2	MAOA	CDC25B	E2F1	KPNA2	RAD21	IGF2
SCNN1A	KCNT2	MT2A	CDCA4	ECT2	MAD2L1	RRM1	IL1R1
SGCG	PPP1R14A	NID2	CDCA8	ELN	MCM2	RRM2	ITM2A
STC1	PROS1	PHACTR2	CDK1	FAM149B1	MCM3	SBSPON	KCNT2
TGFBR2	RGS5	PROS1	CDK2	FAM83D	MCM6	SGCG	METTL7A
	SCNN1A	SCNN1A	CDKN2C	FANCI	MKI67	SHCBP1	NID2
	SGCG	SGCG	CENPA	FEN1	MT2A	SMC4	PCOLCE
	SORBS1	SRGN	CENPE	FKBP5	MTHFD1	STMN1	PDGFD
	STC1	STC1	CENPF	GTSE1	NCAPD2	TACC3	PROS1
	TGFBR2	TGFBR2	CENPU	H2AFV	NCAPG2	TK1	PTGS1
	THBS1	TMTC1	CENPW	H2AFZ	NDC1	TMPO	RGS2
			CEP55	HIST1H4C	NSD2	TOP2A	SCNN1A
			CKAP2	HJURP	NUCKS1	TPX2	SGCG
			CKAP2L	HMGB1	NUF2	TRIP13	SPRY1
			CKAP5	HMGB2	NUSAP1	TUBA1B	STC1
			CKS1B	HMGN2	ORC6	TUBA1C	TGFBR2
			CSE1L	HNRNPA2B1	PCLAF	TUBB4B	
			ANLN	HNRNPD	PCNA	TUBB6	
			ANP32E	HNRNPM	PIMREG	TYMS	
			ARL6IP1	IGF2	PLK1	UBE2C	
			ASF1B	KIF11	PRC1	UBE2S	
			ASPM	KIF20A	PROS1	UBE2T	
			ATAD2	CTHRC1	PRR11	UHRF1	
			AURKB	DEK	PTMA	ZNF367	
			BIRC5	DEPDC1	PTTG1	ZWILCH	
				DHFR	RACGAP1	ZWINT	

Table S5: Donor age and sex for aortic valve specimens. Related to STAR★METHODS: Experimental model and subject details.

Tissue specimen identifier	Donor age	Donor sex	Type of tissue	Calcified aortic valve disease
AOV201	69	MALE	Aortic valve leaflet	YES
AOV339	57	MALE	Aortic valve leaflet	YES
AOV337	68	FEMALE	Aortic valve leaflet	YES
AOV336	75	MALE	Aortic valve leaflet	YES
AOV334	57	MALE	Aortic valve leaflet	YES
AOV278	57	MALE	Aortic valve leaflet	YES
AOV322	72	MALE	Aortic valve leaflet	YES
AOV314	65	MALE	Aortic valve leaflet	YES
AOV307	70	FEMALE	Aortic valve leaflet	YES
AOV297	66	FEMALE	Aortic valve leaflet	YES
AOV298	75	FEMALE	Aortic valve leaflet	YES
AOV294	68	MALE	Aortic valve leaflet	YES
AOV289	55	MALE	Aortic valve leaflet	YES
AOV285	77	FEMALE	Aortic valve leaflet	YES
AOV284	74	FEMALE	Aortic valve leaflet	YES
AOV283	69	MALE	Aortic valve leaflet	YES
AOV275	67	MALE	Aortic valve leaflet	YES
AOV274	78	MALE	Aortic valve leaflet	YES
AOV259	75	MALE	Aortic valve leaflet	YES
AOV250	81	FEMALE	Aortic valve leaflet	YES
AOV242	67	MALE	Aortic valve leaflet	YES
AOV239	78	MALE	Aortic valve leaflet	YES
AOV230	77	FEMALE	Aortic valve leaflet	YES
AOV229	64	MALE	Aortic valve leaflet	YES
AOV222	61	MALE	Aortic valve leaflet	YES
AOV011	41	MALE	Aortic valve leaflet	YES
AOV007	60	MALE	Aortic valve leaflet	YES
AOV391	68	FEMALE	Aortic valve leaflet	YES
AOV012	82	MALE	Aortic valve leaflet	YES
AOV013	71	MALE	Aortic valve leaflet	YES
AOV018	62	FEMALE	Aortic valve leaflet	YES
AOV019	59	MALE	Aortic valve leaflet	YES
AOV020	45	MALE	Aortic valve leaflet	YES
AOV025	56	FEMALE	Aortic valve leaflet	YES
AOV350	78	MALE	Aortic valve leaflet	YES
AOV385	66	MALE	Aortic valve leaflet	YES
AOV382	68	MALE	Aortic valve leaflet	YES
AOV379	63	FEMALE	Aortic valve leaflet	YES
AOV539	Unknown	Unknown	Aortic valve leaflet	NO, normal, autopsy-sourced
AOV561	Unknown	Unknown	Aortic valve leaflet	NO, normal, autopsy-sourced
AOV566	Unknown	Unknown	Aortic valve leaflet	NO, normal, autopsy-sourced
AOV568	Unknown	Unknown	Aortic valve leaflet	NO, normal, autopsy-sourced
AOV559	Unknown	Unknown	Aortic valve leaflet	NO, normal, autopsy-sourced
AOV560	Unknown	Unknown	Aortic valve leaflet	NO, normal, autopsy-sourced
AOV006	Unknown	Unknown	Aortic valve leaflet	NO, normal, autopsy-sourced
AOV628	Unknown	Unknown	Aortic valve leaflet	NO, normal, autopsy-sourced
Lonza 00225974, Lot# 1F5069	41	FEMALE	Aortic valve leaflet cells	NO, normal, live cells
Lonza CBS-58004A	46	FEMALE	Aortic valve leaflet cells	NO, normal, live cells